1
Molecular Simulation of Polymer Melts and Blends: Methods, Phase Behavior, Interfaces, and Surfaces

Peter Virnau, Kurt Binder, Hendrik Heinz, Torsten Kreer, and Marcus Müller

1.1
Introduction

Understanding thermodynamic properties, including also the phase behavior of polymer solutions, polymer melts, and blends, has been a long-standing challenge [1–7]. Initially, the theoretical description was based on the lattice model introduced by Flory and Huggins [1–7]. In this model, a flexible macromolecule is represented by a (self-avoiding) random walk on a (typically simple cubic) lattice, such that each bead of the polymer takes one node of the lattice, and a bond between neighboring beads of the chain molecule takes a link of the lattice. For a binary polymer blend (A,B), two types of chains occur on the lattice (and possibly also "free volume" or vacant sites, which we denote as V). The model (normally) does not take into account any disparity in size and shape of the (effective) monomeric units of the two partners of a polymer mixture. Between (nearest neighbor) pairs AA, AB, and BB of effective monomers, pairwise interaction energies, ε_{AA}, ε_{AB} and ε_{BB}, are assumed. Thus, this model disregards all chemical detail (as would be embodied in the atomistic modeling [8–10], where different torsional potentials and bond-angle potentials of the two constituents can describe different chain stiffness).

Despite the simplicity of this lattice model, it is still a formidable problem of statistical mechanics, and its "numerically exact" treatment already requires large-scale Monte Carlo simulations [11–13]. Consequently, the standard approach has been [1–7] to treat this Flory–Huggins lattice model in mean-field approximation, which leads to the following expression for the excess free energy density of mixing [4]:

$$\frac{\Delta F}{k_B T} = \frac{\phi_A \ln \phi_A}{N_A} + \frac{\phi_B \ln \phi_B}{N_B} + \phi_V \ln \phi_V + \chi_{AB}\phi_A\phi_B + \tfrac{1}{2}\chi_{AA}\phi_A^2 + \tfrac{1}{2}\chi_{BB}\phi_B^2. \tag{1.1}$$

Here ϕ_A, ϕ_B and $\phi_V = 1-\phi_A-\phi_B$ are the volume fractions of monomers of type A, B and of vacant sites, respectively. Every lattice site has to be taken by either

Encyclopedia of Polymer Blends, Volume 1: Fundamentals. Edited by Avraam I. Isayev

ISBN: 978-3-527-31929-9

an A monomer, a B monomer, or a vacancy, and for simplicity the (fixed) lattice spacing is taken as our unit of length. N_A and N_B are chain lengths of the two types of polymers (we disregard possible generalizations that take polydispersity into account [5]). Thus, the first three terms on the right-hand side of Eq. (1.1) represent the entropy of mixing terms, while the last three terms represent the enthalpic contributions (χ_{AB}, χ_{AA} and χ_{BB} are the phenomenological counterparts of the pairwise interaction energies ε_{AB}, ε_{AA} and ε_{BB}, respectively). Note that in the entropic terms the (translational) entropy of a polymer is reduced by a factor $1/N$ in comparison to a corresponding monomer because of chain connectivity. In deriving this simple expression for the entropy, the fact that polymer chains on the lattice cannot intersect either themselves or other chains has not been explicitly taken care of: the excluded volume constraint is only taken into account via the constraint that a lattice site can be taken by at most one monomer, but only the average occupation probabilities ϕ_A, ϕ_B and not the local concentrations c_i^A, c_i^B of a lattice site i enter: while $c_i^A = 1$ or 0 and $c_i^B = 1$ or 0, $\phi_A = \langle c_i^A \rangle_T$, $\phi_B = \langle c_i^B \rangle_T$. By $\langle Q \rangle_T$ we denote a thermal average of an observable Q in the sense of statistical mechanics at a given temperature, T, that is:

$$\langle Q \rangle_T = (1/Z) \sum_C Q(C) \exp\left[-E(C)/k_B T\right] \tag{1.2}$$

$$Z = \sum_C \exp\left[-E(C)/k_B T\right], \quad F = -k_B T \ln Z \tag{1.3}$$

where the sums are extended over all configurations C ("microstates") of the considered statistical system, $E(C)$ is the corresponding energy function (the "Hamiltonian" of the system [4, 9, 10]), and Z its partition function.

From these definitions it should be clear that in the exact expression for the enthalpy one should expect terms of the type:

$$\chi_{AB} \left(\frac{1}{2q}\right) \sum_{j(\text{n.n. of } i)} \left(\langle c_i^A \, c_i^B \rangle_T + \langle c_i^B c_j^A \rangle \right)$$

where q is the number of nearest neighbors of a site i on the lattice, rather than $\chi_{AB}\phi_A\phi_B$. The latter expression results, of course, if this correlation function is factorized, $\langle c_i^B \, c_j^A \rangle_T \approx \langle c_i^A \rangle \langle c_j^B \rangle = \phi_A \phi_B$. This neglect of correlations in the occupancy of lattice sites would become accurate in the limit $q \to \infty$, but turns out to be rather inaccurate for the simple cubic lattice, which has $q = 6$ only. Moreover, as far as unmixing of a polymer blend is concerned, only interchain contacts and not intrachain contacts contribute (strongly attractive intrachain interactions can cause contraction or even collapse of the random coil configurations).

We shall not discuss Eq. (1.1) further for the general case, but rather focus on the two most important special cases, namely incompressible blends and incompressible polymer solutions. Taking $\phi_V = 0$ one can reduce Eq. (1.1) to a simpler expression [1–4], where $\phi_A = \phi$, $\phi_B = 1 - \phi$:

$$\frac{\Delta F}{k_B T} = \frac{\phi \ln \phi}{N_A} + \frac{(1-\phi) \ln (1-\phi)}{N_B} + \chi \phi \, (1-\phi) \tag{1.4}$$

where in the mean-field approximation the Flory–Huggins parameter χ is related to the pairwise energies by:

$$\chi = q\,[\varepsilon_{AB} - (\varepsilon_{AA} + \varepsilon_{BB})/2]/k_B T \tag{1.5}$$

As an example for the predictions that follow from Eqs. (1.4) and (1.5), we note that the stability limit ("spinodal curve") of the homogenous phase is given by the vanishing of the second derivative of ΔF with respect to ϕ:

$$\partial^2(\Delta F/k_B T)/\partial\phi^2 = 0 \tag{1.6}$$

which yields the equation:

$$\chi = \chi_s(\phi) = \{[\phi N_A]^{-1} + [(1-\phi)N_B]^{-1}\}/2 \tag{1.7}$$

Equation (1.7) describes the spinodal curve in the plane of variables (χ, ϕ). The maximum of the spinodal curve for such a binary incompressible mixture yields the critical point, that is:

$$\phi^{crit} = \left(\sqrt{N_A/N_B} + 1\right)^{-1},\ \chi_{crit}^{-1} = 2\left(N_A^{-1/2} + N_B^{-1/2}\right)^{-2} \tag{1.8}$$

For the simplest case of a symmetric mixture ($N_A = N_B = N$), this reduces to $\phi^{crit} = \frac{1}{2}$, and $\chi_{crit} = 2/N$.

The case of an incompressible polymer solution results if we interpret B as a solvent molecule in Eq. (1.4) by putting $N_B = 1$ [or alternatively put $\phi_B = 0$ in Eq. (1.1) and reinterpret V as solvent molecule]. However, while for polymer mixtures in the state of dense melts incompressibility is often a reasonable first approximation, for polymer solutions in some cases such an assumption is inadequate, for example, if one uses supercritical carbon dioxide as a solvent for the polymers [7, 14].

When one tries to account for real polymer systems in terms of models of the type of Eqs. (1.1)–(1.8) the situation is rather unsatisfactory; however, when one fits data on the coexistence curve or on $(\partial^2(\Delta F/k_B T)/\partial\phi^2)_T$, the latter quantity being experimentally accessible via small angle scattering, one finds that one typically needs an effective χ-parameter that does not simply scale proportional to inverse temperature, as Eq. (1.5) suggests. Moreover, there seems to be a pronounced ϕ-dependence of χ, in particular for $\phi \to 1$. Near $\phi = \phi^{crit}$, on the other hand, there are critical fluctuations (which have been intensely studied by Monte Carlo simulations [11–13, 15] and also in careful experiments of polymer blends [16–18] and polymer solutions [19]). Sometimes in the literature a dependence of the χ parameter on pressure [18] or even chain length is reported, too. Thus, there is broad consensus that the Flory–Huggins theory and its closely related extensions [20] are too crude as models to provide predictive descriptions of real polymer solutions and blends. A more promising approach is the lattice cluster approach of Freed and coworkers [21–23], where effective monomers block several sites on the lattice and have complicated shapes to somehow "mimic" the local chemical structure. However, this approach requires rather cumbersome numerical calculations, and is still of a mean-field character, as

far as critical phenomena are concerned. We shall not address this approach further in this chapter.

A very popular approach to describe polymer chains in the continuum is the Gaussian thread model [24–26], and if one treats interactions among monomers in a mean-field-like fashion this leads to the so-called "self-consistent field theory" [27–33] of polymers. This theory is an extension of the Flory Huggins theory to spatially inhomogeneous systems (like polymer interfaces or microphases-separated copolymer systems), with respect to the description of the phase diagrams of polymer solutions and blends. However, it still lacks chemical detail and is on a mean-field level; hence we shall not dwell on it further here.

An alternative approach that combines the Gaussian thread model of polymers with liquid-state theory is known as the polymer reference interaction site model (PRISM) approach [34–38]. This approach has the merit that phenomena such as the de Gennes [3] correlation hole phenomena and its consequences are incorporated in the theoretical description, and also one can go beyond the Gaussian model for the description of intramolecular correlations of a polymer chain, adding chemical detail (at the price of a rather cumbersome numerical solution of the resulting integral equations) [37, 38]. An extension to describe the structure of colloid–polymer mixtures has also become feasible [39, 40]. On the other hand, we note that this approach shares with other approaches based on liquid state theories the difficulty that the hierarchy of exact equations for correlation functions needs to be decoupled via the so-called "closure approximation" [34–38]. The appropriate choice of this closure approximation has been a formidable problem [34–36]. A further inevitable consequence of such descriptions is the problem that the critical behavior near the critical points of polymer solutions and polymer blends is always of mean-field character.

There have been many other attempts to base the description of polymer solutions, melts, and blends on liquid-state theory (e.g., [41–44]) and we shall not mention all of them. Perhaps the most widely used and successful approaches are based on Wertheim's [45, 46] perturbation theory devised to deal with the equation of state of associating fluids. Theories based on this approach, where attractive interactions between different monomers or monomers and solvent particles are treated in first order thermodynamic perturbation theory, often appear under acronyms like TPT1 or SAFT (statistical associating fluid theory). Comparisons with computer simulations [7, 47, 48] have shown that TPT1-MSA [49, 50] (here MSA stands for a closure approximation known [51] as "mean spherical approximation") yields rather reasonable results on phase coexistence, but typically a large overestimation of the two-phase region occurs, and the critical behavior is described as mean-field like; so the correct Ising-type criticality [11–15] cannot be described as expected. The latter comment applies to the many variants of SAFT (e.g., [52–56]) as well. However, as a caveat, apart from this shortcoming and other systematic errors resulting from the fact that thermodynamic perturbation theory [57] becomes generally inadequate at low temperatures and errors from the closure approximations [51] occur, we mention that some variants of such theories invoke additional uncontrolled approximations that may lead to further

uncontrolled errors. For example, the now rather popular perturbed chain (PC)-SAFT approach [56] relies on an expansion of isotherms as sixth-order polynomials of the monomer density and this may give rise to completely spurious gas–gas and liquid–liquid phase equilibria [58, 59] in the equation of state of a homopolymer, in addition to the standard liquid–gas two-phase region, which is the only physically meaningful phase separation of typical homopolymers at high temperatures.

A general conclusion that can be drawn from this short survey on the many attempts to develop analytical theories to describe the phase behavior of polymer melts, polymer solutions, and polymer blends is that this is a formidable problem, which is far from a fully satisfactory solution. To gauge the accuracy of any such approaches in a particular case one needs a comparison with computer simulations that can be based on exactly the same coarse-grained model on which the analytical theory is based. In fact, none of the approaches described above can fully take into account all details of chemical bonding and local chemical structure of such multicomponent polymer systems and, hence, when the theory based on a simplified model is directly compared to experiment, agreement between theory and experiment may be fortuitous (cancellation of errors made by use of both an inadequate model and an inaccurate theory). Similarly, if disagreement between theory and experiment occurs, one does not know whether this should be attributed to the inadequacy of the model, the lack of accuracy of the theoretical treatment of the model, or both. Only the simulation can yield "numerically exact" results (apart from statistical errors, which can be controlled, at least in principle) on exactly the same model, which forms the basis of the analytical theory. It is precisely this reason that has made computer simulation methods so popular in recent decades [58–64].

Consequently, we focus here on computer simulations exclusively. The outline of the remainder of this chapter is as follows: Section 1.2 presents on overview of polymer models (from lattice models to atomistic descriptions) and will also describe the most important aspects of Monte Carlo simulations of these models. As an example, recent work on simple short alkanes and solutions of alkanes in supercritical carbon dioxide [47, 48] will be presented, to clarify to what extent a comparison of Monte Carlo results on phase behavior and experimental data is sensible, and which experimental input into the models is indispensable to make them predictive.

In Section 1.3 we continue the discussion of Monte Carlo simulations of polymer blends and polymer solutions, but with the emphasis on interfaces that result in the context of phase separation: interfaces between coexisting phases in the bulk (liquid–liquid interfaces in a blend, liquid–vapor-type interfaces in a solution) and at solid external walls. It will be shown how all the surface free energies entering Young's formula for the contact angle of droplets can be determined, and how one can estimate the location of wetting transitions. Coarse-grained models are the focus of this section.

Section 1.4 discusses the basic aspects of molecular dynamics simulation of polymer melts and blends with both coarse-grained and chemically detailed models. While the first part of this section emphasizes the basic aspects of the technique, Section 1.4.2 emphasizes non-equilibrium aspects such as the response to shear deformation, and the special techniques necessary to simulate such phenomena

(non-equilibrium molecular dynamics, NEMD). Since shear deformations create heat, the proper thermostating of the system in the context of a NEMD simulation needs to be carefully considered, and this will be explained in this section. Of course, the processing of polymer solutions, melts, and blends in their molten state is always an indispensable step prior to the production of (typically solid) polymeric materials, and hence addressing such problems by the theoretical modeling is clearly adequate and necessary.

While most sections in this chapter emphasize coarse-grained models, it must be stressed that such models can elucidate qualitative trends, but a quantitative prediction of properties of specific polymeric materials is not achieved. The latter task is attempted by molecular dynamics simulations of chemically realistic atomistic models (Section 1.5). Although the feasibility of this "brute force" approach is limited due to excessive demands of computer resources to equilibrate melts of macromolecules with high molecular weights, and there are also uncertainties about the force fields, nevertheless various encouraging results have been obtained, and some examples of them will be reviewed in this section. The "mapping" between atomistic and coarse-grained models will be discussed briefly.

Finally, Section 1.6 gives a short summary of the state of the art and outlook on closely related problems that were not covered in this chapter.

1.2 Molecular Models for Polymers and Monte Carlo Simulations

1.2.1 Modeling Polymers in Molecular Simulations

If generic properties of polymers need to be determined, it is often sufficient to rely on lattice models. For comparison with experiments of particular melts and blends, more sophisticated off-lattice models are typically applied. These models are described by force fields that determine the interactions between atoms or groups of atoms, and the quality of the modeling is essential for the predictive quality of the simulations. Force field parameters can be derived from direct comparison with experimental data, from quantum mechanical calculations, or both. In the first part of this section, we present generic polymer models that are commonly used in molecular simulations without focussing on any particular substance. Emphasis is placed on lattice and simple off-lattice models that will also be discussed in the next three sections. Section 1.5 is dedicated to chemically realistic descriptions.

The first model that took into account excluded volume effects was the self-avoiding-walk (SAW), which was introduced about 60 years ago [65, 66]. Each monomer occupies a lattice site on a simple cubic lattice. The bond length between adjacent monomers is fixed by the lattice constant and the bond angles are restricted by the geometry of the lattice. This model is well-suited to describe generic polymers in dilute, good solvent conditions and exhibits the correct scaling behavior

($R_g^2 \propto N^{2\nu}$, $\nu \approx 0.588$). Variations of this model, like the interacting SAW (iSAW), allow for interactions between non-adjacent beads and can even undergo a phase transition to a globular state, reproducing the generic behavior of a single chain under bad solvent conditions. A particularly popular extension of the iSAW to two types of beads is even able to describe generic properties of proteins. In the HP (hydrophobic–polar) model [67], non-adjacent hydrophobic beads attract each other, whereas interactions between hydrophobic and polar beads and between two polar beads are restricted to excluded volume. These simple conditions suffice to form a hydrophobic core as observed in crystal structures of proteins. Likewise, polymer blends can be readily implemented in such simple models if we allow for a second type of chains and specified interactions between monomers of like and unlike species. Polymers on a simple cubic lattice exhibit two major disadvantages. On the one hand, both bond length and bond angles are fixed and, on the other hand, Monte Carlo simulations on the simple cubic lattice are often plagued with ergodicity problems [68]. The bond fluctuation model [69] was introduced to address these issues while preserving the computational efficiency of lattice models. Again, the basic idea is simple: instead of occupying a simple lattice site, a monomer now occupies a whole lattice cell. Neighboring beads are only allowed to move such that the bond does not stretch or compress too much. Specifically, bond vectors are chosen to prevent overlaps of adjacent monomers and intersection of bonds during simulation. Note that, due to this additional flexibility, the bond fluctuation model already resembles to some extent a coarse-grained continuum model.

A simple and very popular example of a coarse-grained off-lattice model is given by the bead-spring chain of Kremer and Grest [70, 71]. In this model monomers interact via a Lennard-Jones potential:

$$V_{\mathrm{LJ}}(r) = \begin{cases} 4\varepsilon\left[\left(\frac{\sigma}{r}\right)^{12} - \left(\frac{\sigma}{r}\right)^{6} + \text{const.}\right], & \text{if } r < r_c \\ 0, & \text{else} \end{cases} \tag{1.9}$$

To increase computational efficiency the Lennard-Jones potential usually is cut and shifted at either twice the minimum value, or 2.5σ. The constant in Eq. (1.9) is chosen such that V_{LJ} is continuous at $r = r_c$. The value of ε sets the scale of energy (and temperature T, which is often normalized as $T^* = k_B T/\varepsilon$), and the size σ of effective monomers sets the scale of length. In addition, adjacent beads interact with the so-called FENE potential:

$$V_{\mathrm{FENE}}(r) = -\text{const.} \cdot \varepsilon \cdot \ln\left[1 - \left(\frac{r}{r_{\max}}\right)^2\right] \tag{1.10}$$

Constants in Eq. (1.10) are chosen such that the most favorable distance between bonded monomers is slightly smaller than the distance between non-bonded monomers to prevent crystallization. Alternatively, a harmonic potential can be used for bonded monomers instead of Eqs. (1.9, 1.10). As indicated for lattice models, polymer blends can be implemented by adjusting the interaction strength ε for monomers of

type A and B and between A and B. By mapping ε and σ to experimental energy and length scales, simulations of this model can be compared with experiments of specific polymers. In these scenarios, single Lennard-Jones beads typically represent groups of carbon atoms [47].

The next steps towards a more chemically detailed description are so-called united atom models. In this class hydrogen atoms are grouped together with the heavier atoms to which they are attached. These potentials typically contain both bond bending and torsional terms. Fully atomistic models, which frequently are used in simulations of biopolymers [72], consider hydrogen as a separate particle and often contain electrostatic terms as well. Section 1.5 presents a few selected examples of atomistic polymer models in comparison with experiments.

At the end of this introductory section we emphasize that the model should be adequate for the problem in question. Adding additional parameters to describe the system in a chemically realistic manner increases the computational cost and does not necessarily lead to better agreement with experiments. This should be considered, especially because on today's computers fully atomistic molecular dynamics simulations are typically limited to box sizes of a few nanometers and 10s or 100s of nanoseconds of simulated time.

1.2.2 Basics of Monte Carlo Simulations

Classical molecular simulations are dominated by two classes of algorithms: Monte Carlo and molecular dynamics [62, 63]. Monte Carlo generally aims at generating independent configurations of a statistical system that contributes to the Boltzmann-weighted statistical average of an observable. This information can also be obtained from molecular dynamics simulations in which a starting configuration is evolved according to Newton's equations of motion. In addition, molecular dynamics generates information about the dynamical evolution of a system. In the following, we give a short overview and present a selection of several techniques important for studying polymer blends and melts. After a brief introduction to basic Monte Carlo algorithms we focus on grand-canonical simulations, which are commonly used to determine phase diagrams of polymer melts and blends. Molecular dynamics simulations are introduced in Section 1.4.

Monte Carlo simulations are, as indicated by the name, based on the idea of evolving a system by drawing random numbers. Unfortunately, statistically meaningful configurations are typically confined to a small volume of phase space. To evolve a system within this volume we apply importance sampling, that is, we only sample states that actually contribute to statistical averages.

To derive the relevant equations we consider our system to be in a particular state *i*. This state is in equilibrium with its environment if the probability flows in and out of this state are equal:

$$\sum_j P(i) a_i \omega_{ij} = \sum_j P(j) a_j \omega_{ji} \quad \forall j \tag{1.11}$$

where $P(i)$ is the probability of residing in state i, which is typically given by the Boltzmann distribution;
ω_{ij} is the probability of jumping from i to j as given by the algorithm;
$a_{i,j}$ is the probability of selecting or placing a particular particle for the move.

The system is in equilibrium if Eq. (1.11) applies to all states. Equation (1.11) is always fulfilled if the stricter condition:

$$P(i)a_i\omega_{ij} = P(j)a_j\omega_{ji} \quad \forall i,j \tag{1.12}$$

is met, which is known as detailed-balance. Several ways to fulfill detailed-balance are conceivable. The Metropolis criterion [83] was historically the first implementation of detailed balance, and remains by far the most popular choice today:

$$w_{ij} = \min\left(1, \frac{a_j P_j}{a_i P_i}\right). \tag{1.13}$$

For example, consider a local Monte Carlo scheme for a Lennard-Jones liquid in the NVT (constant particle number, volume, and temperature) ensemble: We choose one particle at random, and move it a fixed distance away from the previous position in an arbitrary direction. For the reverse move (from j to i) $a_j = a_i$ the two prefactors cancel out. $P_i \propto \exp[-\beta E(i)]$ according to the canonical Boltzmann distribution. Equation (1.13) indicates that the move is always accepted if the energy of the system is lowered by the displacement. If the energy increases, the move is accepted with probability $\exp(-\beta\Delta E)$, that is, we draw a random number between 0 and 1 and accept the move if the random number is smaller than $\exp(-\beta\Delta E)$.

Apart from local displacements, a wide variety of Monte Carlo moves can already be formulated using Eq. (1.13). For instance, an end-monomer can be cut from a polymer chain and reattached at the other end. In this case the movement of the chain resembles a slithering snake, from which the name of the algorithm is derived [73, 74]. In dilute systems, a monomer can be selected at random, around which one side of the polymer is rotated by an arbitrary angle (or an angle allowed by the lattice geometry). This so-called pivot algorithm is currently the most efficient way to simulate single chains in good solvent conditions [75, 76]. For globular states, various end- [77] and internal-rebridging [78, 79] algorithms have been developed in which the chain is cut and reconnected internally. A version that cuts and rebridges two chains in a melt also exists [80]. From this list it becomes immediately clear that Monte Carlo moves do not have to mimic physically feasible moves of a real polymer chain. This characteristic is oftentimes advantageous as it allows for a fast and efficient sampling of configuration space. On the downside, information about the physical evolution of the system is lost.

1.2.3 Determination of Phase Behavior

In the following, we focus on a set of techniques commonly used to determine the phase behavior of oligomer melts [47, 48] and blends [81] to give an example of how

MC techniques are applied in practice. The methodology is rather general and in principle can be applied to any molecular liquid [82] or spin system. It also has advantages over techniques like Gibbs ensemble Monte Carlo [83] because it can be combined with finite-size scaling in the vicinity of the critical point. In addition, the method yields interfacial properties. Our presentation follows Reference [47]. Simulations are typically performed in the grand canonical μVT ensemble with periodic boundary conditions, that is, we fix the chemical volume and temperature but allow for particle insertions or deletions. For a simple Lennard-Jones liquid, Eq. (1.13) becomes:

$$w_{ij} = \min\left(1, \frac{V}{n+1}\exp\left(-\beta\Delta E + \beta\mu\right)\right) \tag{1.14}$$

for insertion from n particles to $n+1$ particles in the system, and:

$$w_{ji} = \min\left(1, \frac{n}{V}\exp\left(+\beta\Delta E - \beta\mu\right)\right) \tag{1.15}$$

for deletion attempts from n to $n-1$; V denotes the volume of the simulation box. The simulation of polymer melts is slightly more involved because insertions of whole chains are typically rejected in a melt due to overlaps. To attenuate this problem, more advanced schemes like configurational bias Monte Carlo [85–88] need to be implemented. Again, the basic idea is simple: the first particle is inserted at random. Subsequent particles of the chain are inserted after the surrounding area is scanned for favorable vacancies. The bias, however, has to be considered when final acceptance probabilities are calculated. This algorithm, combined with local updates schemes introduced above, works very well for oligomers. Melts containing larger chains remain challenging and the efficiency of the grand canonical insertion attempt still limits the applicability of the whole approach.

In a typical simulation run, a joint histogram of particle number and energy is accumulated. The system is at coexistence when an unweighted simulation spends an equal amount of time in the coexisting phases. If we plot the probability distribution as a function of particles in the melt, we obtain a double-peaked distribution at coexistence and the areas below the two peaks are equal [88, 90]. Coexistence densities can be calculated by determining the average particle numbers in the gas and the liquid peak and dividing the respective numbers by the volume of the simulation box.

In practice, it is difficult to estimate the coexistence chemical potential ahead of time. However, if two distributions at μ, T and μ', T' overlap sufficiently, it is possible to extrapolate data from μ, T to μ', T' and avoid a second simulation [91]. The probability of a certain configuration c at μ', T' is given by:

$$P_{\mu',T'}(c) = \frac{Z}{Z'} P_{\mu,T}(c) \quad \mathrm{e}^{-(\beta'-\beta)E + (\mu'\beta' - \mu\beta)n} \tag{1.16}$$

where $P_{\mu',T'}(n_0)$ is the sum over all configurations c_i at n_0.

$\sum_{\{c_i\}|n=n_0} P_{\mu,T}(c_i) \propto \sum_{\{c_i\}} \delta(n-n_0)$ can be determined from the original data set. After a suitable normalization, the grand canonical partition sums Z and Z'

disappear and we obtain:

$$P_{\mu',T'}(n_0) = \frac{\sum_{\{c_i\}} \delta(n-n_0) \quad e^{-(\beta'-\beta)E_i + (\mu'\beta'-\mu\beta)n}}{\sum_{\{c_i\}} \quad e^{-(\beta'-\beta)E_i + (\mu'\beta'-\mu\beta)n}} \tag{1.17}$$

From a statistical mechanics viewpoint, molecular systems share several properties with Ising spin systems if density fluctuations are substituted with spin flips. Polymer melts and blends without long-range interactions typically belong to the 3d-Ising universality class [92, 93], and critical points can be determined with techniques that were originally derived for spin systems [94]. To this extent we can calculate second- or fourth-order cumulants [94]:

$$U_2 = \frac{\langle M^2 \rangle}{\langle |M| \rangle^2}, \quad U_4 = \frac{\langle M^4 \rangle}{\langle M^2 \rangle^2} \tag{1.18}$$

which become system size independent and cross at the critical point (Figure 1.1). M denotes the order parameter of the transition. For liquid–vapor phase coexistence it is given by:

$$M \equiv \varrho - \langle \varrho \rangle \tag{1.19}$$

In practice, we perform several simulations close to the critical point for different simulation box volumes and determine the coexistence chemical potential as indicated above. These simulations can be extrapolated to different temperatures close to T_c to obtain $U_K(V,T)(K=2,4)$. The critical point is the intersection point of the cumulants. The computation of cumulants is closely related to finite-size effects [95–97] that haunted computer simulations in the early days but are now under firm control: In a macroscopic system the correlation length diverges at the

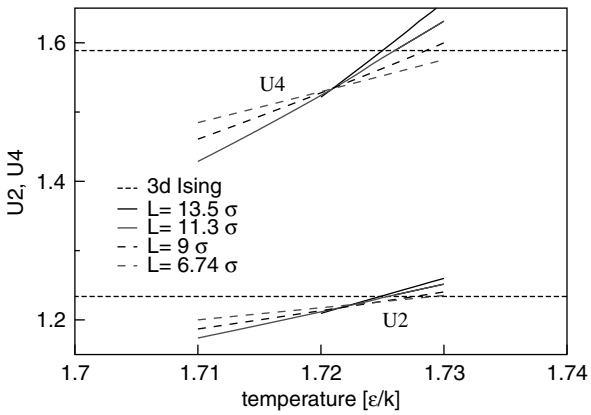

Figure 1.1 Second- and fourth-order cumulants for a LJ + FENE pentamer in comparison to the corresponding values for the 3d Ising distribution at criticality (horizontal straight lines). Each line has been extracted from a single simulation by extrapolating the data set to several temperatures. Adapted from Reference [47].

critical point. In a system of finite size, the correlation length can at most be equal to half of the linear dimension of the simulation box, which has to be considered in the vicinity of T_c. Definition (1.19) is sufficient for most purposes. Note, however, that an exact mapping of fluid criticality to Ising criticality has to consider field-mixing effects [92] and M becomes a linear combination of density and energy. Owing to higher order effects and corrections to scaling the values of U_4 and U_2 at the intersection points of the curves in Figure 1.1 deviate slightly from the asymptotic values obtained for the 3d Ising model (dotted horizontal lines). Note, however, that the intersections of both U_2 and U_4 occur at about the same temperature, which can be determined with good accuracy.

Away from the critical point, that is, at low temperatures, both phases are separated by a free energy barrier that corresponds to a region of low probability. This barrier cannot be overcome by thermal fluctuations. Several sophisticated schemes have been devised to address this issue. Multicanonical methods [98] modify the Hamiltonian in order to sample a range of densities uniformly. To this end, a weight function $w[n]$ is added to the original Hamiltonian. The simulated distribution $P_{\text{sim}}(n) = P(n)\exp(-w[n])$ becomes flat for the choice of $w(n) \approx \ln P(n)$. Unfortunately, $P(n)$ is a priori unknown, but can be estimated by extrapolating an overlapping data set [91]. A sequence of simulations and extrapolations typically starts close to the critical point where barriers between both peaks are small and no weighting is required for the first run. The weight function $w(n)$ can also be self-adjusted during simulation [99–102]. Note, that some of these schemes violate detailed balance and bear the risk of systematic errors. However, they are well-suited to generate an educated guess for the probability distribution, which can be used in a weighted simulation with fixed weights. A detailed discussion of methods to overcome free energy barriers can be found in Reference [103].

In the following we focus on a scheme that is based on umbrella sampling [104] and circumvents most of these problems. In successive umbrella sampling [105] the relevant range of states is subdivided into small windows that are sampled consecutively. This allows us to simulate without a weight function or to generate a weight function on the fly from previous windows by means of extrapolation. In the simplest implementation, we start with an empty box and allow the system to change only between 0 and 1 particle. A histogram $H(n)$ monitors how often each state is visited (n denotes the number of particles in the simulation box). After a predetermined number of insertion/deletion Monte Carlo moves, the ratio $H(1)/H(0)$ is determined, and we move the window to the right (to allow 1 and 2 particles). This procedure is repeated until all relevant states have been sampled. Then, the (unnormalized) probability distribution can be estimated recursively:

$$\frac{P(n)}{P(0)} = \frac{H(1)}{H(0)} \cdot \frac{H(2)}{H(1)} \cdots \frac{H(n)}{H(n-1)} \tag{1.20}$$

or:

$$\ln \frac{P(n)}{P(0)} = \ln \frac{H(1)}{H(0)} + \ln \frac{H(2)}{H(1)} + \cdots + \ln \frac{H(n)}{H(n-1)} \tag{1.21}$$

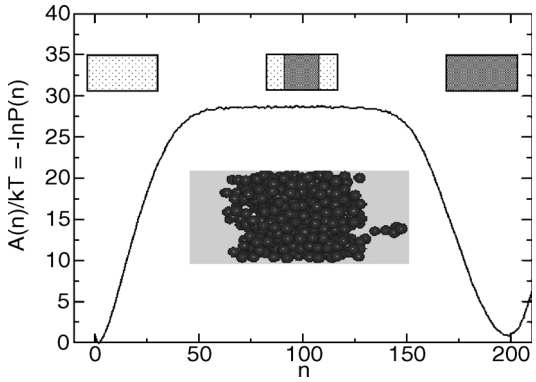

Figure 1.2 Free energy as a function of the number of LJ + FENE pentamers (n) in the simulation box ($T = 1.38\,\varepsilon/k_B$, $V = 9 \times 9 \times 18\,\sigma^3$). Inset: typical configuration for $n = 100$ pentamers. With permission from Reference [47].

Logarithms are used to increase numerical accuracy as probabilities can become very low. The efficiency of the algorithm can be increased by combining the scheme with the multicanonical concept. In a weighted simulation we replace $H(n)$ in Eq. (1.20) by $H(n)\exp[-w(n)]$. After $P(n)$ is determined according to Eq. (1.20), $w(n) = \ln[P(n)]$ is extrapolated to the next window and used as an educated guess for $w(n+1)$.

Once the probability distribution is determined, information about interfacial properties can be extracted. Half way in between the gas and the liquid phase we typically observe configurations in which half of the simulation box is filled with liquid and half of the box is filled with gas at coexistence density (Figure 1.2 inset). As the free energy of the coexisting phases is the same, the difference in free energy can be attributed to the presence of the interface [106]:

$$\gamma = \frac{k_B T}{2L^2} \ln \frac{P(n_{max})}{P(n_{min})} \tag{1.22}$$

The interface area is L^2; the factor of 2 arises from periodic boundary conditions. $P(n_{max})$ is the average height of both peaks and $P(n_{min})$ the minimum in between. For these measurements an elongated box is preferred to ensure that the two interfaces do not interact [107, 108].

Finally, we briefly mention an example that combines a coarse-grained modeling ansatz with grand canonical simulations. In this particular case, hexadecane is modeled as a chain of five coarse-grained Lennard-Jones beads [Eq. (1.9)] that are connected by FENE [Eq. (1.10)] springs [48]. The solvent, carbon dioxide, is represented by a simple Lennard-Jones bead that contains an additional r^{-10} term to account for the (spherically averaged) quadrupolar moment of CO_2 [82, 111]. Simulation parameters ε, σ, and q (for CO_2) are derived by equating the critical temperature, the critical density, and the quadrupolar moment (in the case of CO_2) of simulation and experiment for the pure components. Mixture parameters ε_{AB} and

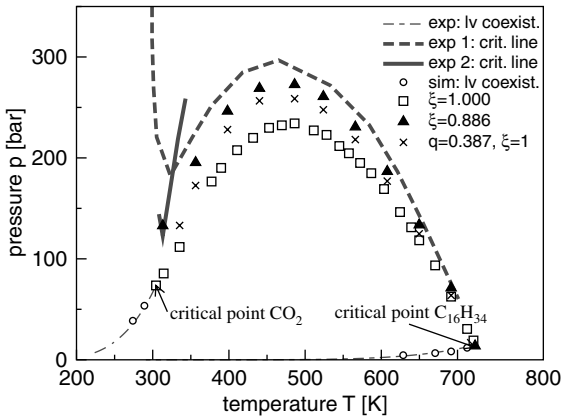

Figure 1.3 Projection of the global mixture phase diagram of a hexadecane–CO_2 mixture onto the pressure–temperature plane. Simulation results for the liquid–vapor coexistence of the pure components are shown by circles. Thick lines mark two different experimental observations of the critical line from References [109, 110]. The thin dash-dotted lines indicate the experimental liquid–vapor coexistence of the pure fluids. Crosses mark the critical mixture line obtained for a CO_2 model that includes a spherically averaged quadrupolar moment, and no modification of the Lorentz–Berthelot mixing rule. Triangles and squares denote the critical line for a CO_2 model without quadrupolar moment with (triangles) and without modification (squares) of the Lorentz–Berthelot rule.

σ_{AB} are given by the Lorentz–Berthelot combining rule ($\varepsilon_{AB} = \xi\sqrt{\varepsilon_A \varepsilon_B}$, $\xi = 1$, $\sigma_A = 0.5(\sigma_A + \sigma_B)$). Figure 1.3 shows a projection of the phase diagram and the critical line onto the pressure–temperature plane. Even though the model is very simple and lacks atomistic details it can describe adequately the phase behavior of the mixture without additional fitting parameters. If, however, the quadrupolar moment of CO_2 is not taken into account, a modification of the Lorentz–Berthelot rule is required ($\xi < 1$). This emphasizes that atomistic detail is not always required to describe the phase behavior correctly. However, it is advisable to include physically relevant quantities like the quadrupolar moment of CO_2.

1.3
Wetting and Phase Diagrams in Confined Geometries

1.3.1
Length and Energy Scales of Minimal, Coarse-Grained Models for Polymer–Solid Contacts

While previous sections have focused on the bulk phase behavior and the properties of interfaces between coexisting bulk phases, the polymer material is often confined in a container or a thin polymer film is supported by a substrate. This confinement

can give rise to wetting phenomena and these effects may profoundly alter the phase behavior in confined geometry [112].

In the following, we assume that the confining walls of the container or the supporting substrate (e.g., a wafer) are hard and non-deformable, that is, the properties of the solid do not change as it is brought into contact with the polymer material. If one measures the density profile of the polymer material at the polymer–solid contact, one will typically observe a steep rise of the density from zero (in the solid, confining wall) to the bulk density of the polymer material. The spatial extension of this polymer–solid interface is only a few ångström, that is, its width is dictated by the size of the atomistic constituents. On the other hand, in multicomponent polymer materials (i.e., polymer blends or polymer–solvent mixtures) one component will enrich at the solid surface, and the width of these enrichment layers may extend far away from the solid surface.

Two different enrichment phenomena can be distinguished [113]:

1) If the multicomponent material is completely miscible in the bulk, then a component will typically adsorb at the preferential, solid surface. This phenomenon alters the composition profile near the polymer–solid contact on a length scale that is set by the molecular extension. The enrichment layers are much larger than the width of the polymer–solid interface but they cannot grow macroscopically large.
2) If the multicomponent material exhibits two coexisting phases in the bulk, then one phase will be enriched at the polymer–solid contact and, provided that the solid is sufficiently preferential, this wetting layer of the preferred phase will grow macroscopically thick. One says that the preferred phase of the polymer material wets the solid [114].

In both situations the polymer–solid interface is much thinner than the width of the enrichment layer or the interphase. Since previous sections have dealt with phase coexistence in multicomponent polymer materials, we restrict ourselves to the wetting phenomena (2) and refer the reader to References [115–117] for simulation studies of adsorption phenomena within the framework of coarse-grained models.

The properties of the polymer–solid interface are most suitably investigated by atomistic modeling approaches. Atomistic modeling can address the complex interactions between polymer and solid materials and study the subtle conformational changes and structuring effects of the polymer liquid in the ultimate vicinity of the solid. However, atomistic approaches cannot address the length and time scales required to build up and equilibrate wetting layers.

Systematic coarse-graining schemes have been applied to one-component polymer melts in contact with solid surfaces. In this framework, one starts with an atomistic modeling approach and systematically devises effective free energies of interaction between coarse-grained segments along the polymer. In this way, information on the atomistic scale may be transferred into coarse-grained models. An interesting example of this strategy is the investigation of polycarbonate at a nickel surface where a strong, specific adsorption of the chain ends to the solid

surfaces has been revealed by atomistic modeling and this specific adsorption has been incorporated in the coarse-grained model [118]. Without the underlying atomistic modeling this specific interactions could have been easily overlooked. This example highlights the (rather special) case of a coupling between atomistic surface properties and long-range conformational properties. Typically, however, the surface tension of a polymer melt exhibits only a weak dependence on molecular weight.

If one uses a coarse-grained approach, one has to identify the relevant properties that the description on the coarser scale has to capture. In the following, we specifically consider wetting phenomena in a binary AB polymer blend that exhibits liquid–liquid phase separation between an A-rich and a B-rich phase. The thermodynamics of the surface enrichment layers is dictated by the free energies of the solid in contact with the two coexisting phases, γ_{AW} and γ_{BW}, and their interfacial tension, γ_{AB}. If the solid surface, W, attracts the A-rich phase, then a domain of the A-rich phase, which is embedded in the B-rich phase, will form a drop at the solid surface. The AB-interface at the boundary of the domain will make the contact angle, Θ, with the solid wall, W. Young's equation describes the balance of forces at the three-phase contact line parallel to the solid surface and dictates [119]:

$$\gamma_{WB} - \gamma_{WA} = \gamma_{AB} \cos \Theta \tag{1.23}$$

Note that the surface tensions, γ_{WB} and γ_{WA}, are large. On the atomistic scale there are strong forces and, consequently, the energy of a segment with the surface can exceed the thermal energy scale, $k_B T$, by far. Moreover, the steep rise in density at the narrow polymer–solid contact gives rise to important changes of the conformational entropy (Lifshitz entropy [27]). In contrast, the interfacial free energy, γ_{AB}, is very small on the length scale of a coarse-grained segment. For a strongly segregated, symmetric binary polymer blend, one obtains [28]:

$$\gamma_{AB} = k_B T \varrho b^2 \sqrt{\chi/6} \tag{1.24}$$

where b denotes the statistical segment length, ϱ the number density of coarse-grained segments, and χ the Flory–Huggins parameter, which describes the repulsion between segments of the different polymer species of the blend.

Typically, the Flory–Huggins parameter is very small, that is, of the order $1/N$. Therefore, the left-hand side of Young's equation, Eq. (1.23), consists of a cancellation of two large contributions. It is a formidable task to predict via atomistic modeling the difference $\Delta\gamma = \gamma_{WB} - \gamma_{WA}$ or the Flory–Huggins parameter, χ with an accuracy of the order $k_B T/N$ per segment.

The behavior of polymer solutions, which exhibit phase coexistence between a polymer-rich liquid (L) and a polymer-poor vapor (V), is qualitatively similar. Only the separation of energy scales between the surface tensions of the polymer and vapor in contact with the solid and the liquid–vapor interfacial tension is less pronounced because the liquid–vapor interface also is narrow and the cohesive van der Waals interactions inside the liquid are strong.

The idea of a minimal coarse-grained model for polymer–solid contacts consists in not describing the structural details of the polymer–solid contact on the length scale of Ångströms because this length scale is not resolved. Instead, the aim is to tailor the interactions at the surface in order to match the difference in surface tension, $\Delta\gamma$, of the coarse-grained model to the experimental data. In this way, the macroscopic interfacial thermodynamics is parameterized.

Another important ingredient, which determines the wetting behavior, is the interaction between the outer, liquid–vapor interface of the wetting layer and the solid surface. This interaction (per unit area) is denoted as the interface potential [114] and it dictates, *inter alia*, the order of the wetting transition and the way, in which the thickness of the wetting layer grows as one approaches the bulk phase coexistence by varying the pressure.

Generally, the interface potential consists of a short-ranged and long-ranged contribution. The short-ranged potential stems from the distortion of the density profile at the interface. It decays exponentially as the thickness of the wetting layer increases and its length scale is set by the decay length in the wings of the interfacial profile, that is, the bulk correlation length, $\xi \sim R_e$.

The long-ranged part of the interface potential arises from the integrated van der Waals interactions inside the polymer material and between the solid surface and the polymer. This long-ranged interaction can be described by an external potential, which decays like [32]:

$$V_{\text{wall}}^{\text{lr}}(z) = \underbrace{\frac{\Delta A}{6\pi\varrho}}_{\varepsilon_{\text{wall}}} \cdot \frac{1}{z^3} \tag{1.25}$$

The strength, $\varepsilon_{\text{wall}}$, is parameterized by the Hamaker constant, A, which is proportional to the energy parameter, ε, of the Lennard-Jones potential. Typically, in a coarse-grained model, the Lennard-Jones interactions are cut-off at a finite distance, cf. Eq. (1.9). Therefore, the strength, ΔA, is the difference between the Hamaker constant of the interactions inside the polymer liquid and that between polymer and solid.

To describe the thermodynamics and structure of wetting layers at a polymer–solid contact within the framework of a minimal, coarse-grained model, one has to identify the bulk properties, Flory–Huggins parameter, χN, the mean-squared end-to-end distance, R_e, and the molecular density, ϱ/N. R_e characterizes the gross features of the molecular shape on large length scales, and χN and ϱ/N can be identified, for example, by matching the critical point of the blend or solution to experimental data. The structure and thermodynamics of the polymer–solid contact requires (at least) two additional, coarse-grained parameters – the difference in the surface tension, $\Delta\gamma$, between the two coexisting phases and the strength of the long-ranged interactions. The former can be identified by the macroscopic contact angle that a drop of the A-rich phase or polymer-rich phase embedded in a B-rich matrix or vapor makes with the solid surface. The latter can be estimated from experimental data on the Hamaker constants.

1.3.2
Measuring the Surface Free Energy Difference, $\Delta\gamma$, by Computer Simulation

Here we discuss how to determine the additional coarse-grained parameters that characterize the coarse-grained model of the polymer–solid contact using the example of a one-component polymer material, which exhibits liquid–vapor phase coexistence. Knowing the bulk phase behavior and the interfacial tension between the coexisting phases, one could determine the difference, $\Delta\gamma$, by measuring the contact angle of a cap-shaped drop on the solid surface. This procedure mimics the experimental measurement but, unfortunately, the small droplet sizes accessible in simulations gives rise to significant finite-size effects:

1) If a drop is formed on the surface, the chemical potential of the system will be shifted away from the bulk coexistence value (Kelvin equation). Drops of a given size are only stable for a certain range of system sizes. If the system size is too large, the system will rather dissolve the excess material homogeneously in the volume than pay the free energy cost of the liquid–vapor interface [121]. This is the analog of the droplet condensation–evaporation transition in the bulk [122].
2) The contact angle of a small droplet may significantly be affected by the effects of the line tension that describes the free energy costs of the three-phase contact between liquid, vapor, and solid. This effect can be greatly reduced by considering cylindrical droplets that span the simulation box in one direction via the periodic boundary condition. In this case, the length of the three-phase contact line is twice the width of the system independent from the droplet size or contact angle [123].
3) The contact angle is defined by the asymptotic behavior of the liquid–vapor interface approaching the surface. At short distances from the surface, the interaction between the interface and the surface – the interface potential – distorts the interface away from its asymptotics and, thus, it may be very difficult to identify the asymptotic behavior from simulation data of small drops [31].

These difficulties will be avoided if one directly computes the surface free energy difference. To measure surface free energies, we apply the same grand-canonical Monte Carlo technique that we used for the bulk thermodynamics (Section 1.2.3), now in the presence of two surfaces [120, 124]. We fix the chemical potential to its coexistence value and, using the re-weighting method, we can make the simulation sample all densities between the vapor phase (V) and the liquid phase (L) in contact with the surface. Again the logarithm of the probability distribution, P, yields the free energy as a function of the density. Figure 1.4 displays the results for the Lennard-Jones bead-spring model with $N = 10$ effective segments at temperature $k_B T/\varepsilon = 1.68$. The free energy exhibits two minima, corresponding to configurations where either a vapor (low density) or a liquid (high density) phase is in contact with the surface. The ratio of the probability for finding the system in one of these phases yields the difference

in the surface free energies:

$$\Delta\gamma \equiv \gamma_{VW} - \gamma_{LW} = \frac{k_B T}{2L^2} \ln\left[\frac{P(\phi_L)}{P(\phi_V)}\right] \tag{1.26}$$

where $2L^2$ denotes the area of the two surfaces. Note that the bulk does not yield any contribution to the difference because, at coexistence, the grand-canonical free energies (i.e., pressure) of the two coexisting phases – liquid and vapor – are identical.

At intermediate densities the typical conformations consist of a liquid slab at each wall. If the system size is sufficiently large the distance between the liquid–vapor interfaces and the wall and their mutual distance become large. In this limit the interfaces neither interact with the walls nor with each other, and we expect only a weak dependence of the free energy on the density, that is, a plateau in the probability distribution, P, at intermediate values of the average density. The liquid will wet the surface if the difference in surface tensions equals the interfacial tension, $\Delta\gamma = \gamma_{LV}$. In a sufficiently large system, the wetting transition corresponds to the point where the plateau value of P equals $P(\phi_V)$.

For the system size studied in Figure 1.4, we do not observe a plateau, that is, once the interfaces have reached a distance from the wall, which is large enough

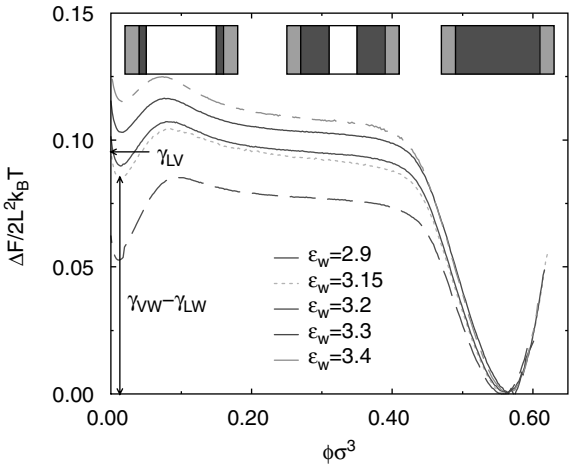

Figure 1.4 Illustration of the simulation technique for a one-component, bead-spring model at temperature $k_B T/\varepsilon = 1.68$ and μ_{coex}. A cuboidal system geometry $13.8\sigma \times 13.8\sigma \times 27.6\sigma$ with periodic boundary conditions in the two short directions and two confining surfaces in the long direction is used. The curves are shifted such that the free energy of the liquid phase vanishes. The horizontal arrow on the left marks the value of the interfacial tension γ_{LV}, while the vertical arrow marks the difference in the surface tension between the vapor/wall and liquid/wall for $\varepsilon_w = 3.15$. Typical system configurations are sketched schematically. Adapted from Reference [120].

for the interface potential between the interface and the surface to decay, they already begin to interact mutually. This indicates that our simulation cell is too small to accommodate two non-interacting solid–liquid and liquid–vapor interfaces. Nevertheless, we can reliably determine $\gamma_{VW} - \gamma_{LW}$. In these limiting states, the container is either completely filled with vapor or liquid, and there are no liquid–vapor interfaces present. The perturbation of the density profile in the liquid extends only over a few segmental diameters, σ, which is much smaller than the extension of the simulation cell.

To parameterize the coarse-grained model to a specific physical realization, one has to tune the interactions, V_{wall}, between solid and polymer to reproduce the experimental value of the surface free energy difference, $\Delta\gamma$. Once $\Delta\gamma$ has been obtained via the method described above for a particular strength, ε_{wall}, of V_{wall}, the dependence on the attractive strength of the wall can be obtained via thermodynamic integration [120, 124]:

$$\Omega(\varepsilon_{wall}) = \Omega(\varepsilon_o) + \int_{\varepsilon_o}^{\varepsilon_{wall}} d\varepsilon_{w'} \frac{\langle E_{wall}(\varepsilon_{w'})\rangle}{\varepsilon_{w'}} \tag{1.27}$$

where Ω is the grand canonical potential and $E_{wall} = L^2 \int dz\, \phi(z) V_{wall}(z)$ denotes the interaction energy associated with the monomer–wall interaction potential. Like any thermodynamic integration, this procedure can be efficiently carried out in the framework of an expanded ensemble.

1.3.3
Application to Polymer–Solvent Mixtures

To illustrate these techniques, we consider the coarse-grained model for hexadecane and carbon dioxide, which we have discussed in Section 1.2. The correction of the Lorentz–Berthelot rule is set to $\xi = 0.9$ and the temperature is fixed at $k_B T/\varepsilon = 0.92$. (In this case carbon dioxide was modeled as a simple Lennard-Jones bead without quadrupolar moment.) The short- and long-ranged interactions at the polymer–solid contact are described by a 9-3-potential of the form:

$$V_{wall} = \varepsilon_{WS(P)} \left[\left(\frac{\sigma_{S(P)}}{\Delta z} \right)^9 - \left(\frac{\sigma_{S(P)}}{\Delta z} \right)^3 \right] \tag{1.28}$$

where ε_{WS} and ε_{WP}, denote the strength of the surface interaction acting on solvent and polymer, respectively.

Using the technique illustrated in Figure 1.4 for the one-component system, one can accurately locate the strength of the surface interaction, ε_{WP}^{wet}, at which the polymer film will wet the substrate, as a function of the vapor pressure, P. Figure 1.5 depicts the results for different values of the attraction, ε_{WS}, of the substrate to the solvent, carbon dioxide. If the substrate does not strongly attract the solvent, increasing the vapor pressure, P will stabilize the polymer film because of the concomitant decrease of the liquid–vapor interfacial tension, γ_{LV}. If the substrate strongly attracts the solvent, however, the solvent will form a layer at the substrate and will displace the

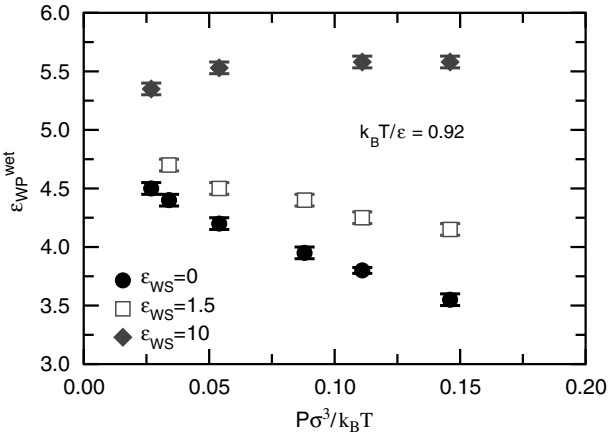

Figure 1.5 Dependence of the wetting transition ε_{WP}^{wet} on pressure, P, estimated by grand-canonical Monte-Carlo simulations of a polymer–solvent mixture. Adapted from Reference [125].

polymer. The excess of solvent at the surface may lead to dewetting of the polymer film upon increasing the pressure. This effect has also been corroborated by self-consistent field calculations [125, 126].

1.4
Molecular Dynamics Method

1.4.1
Basic Molecular Dynamics

Molecular dynamics [127] (MD) is a numerical technique to approximate the static and dynamic properties of classical many-body systems. MD techniques are commonly employed alongside Monte Carlo techniques because dense packing reduces the acceptance probability of translation and chain rotation moves to very low values, particularly when using all-atom models.

The key idea is simple: if $U(\{\boldsymbol{r}_i\})$ is the total potential acting on particle i with mass m_i and position $\boldsymbol{r}_i(t)$ at time t, then Newton's equations of motion (EOM):

$$m_i \frac{\partial^2}{\partial t^2} \boldsymbol{r}_i(t) = -\nabla_i U(\{\boldsymbol{r}_i\}) \tag{1.29}$$

are solved iteratively. The main justification of the MD method is based on the ergodic hypothesis that time averages are equal to statistical ensemble averages. However, MD simulations generate cumulative errors that cannot be suppressed entirely, but are minimized using adequate integration schemes. Various algorithms have been suggested to solve Eq. (1.29).

The Verlet algorithm uses the Taylor expansions of the position vectors in different time directions. With Δt the "time-step" of the simulation, adding the expansions for $\boldsymbol{r}_i(t+\Delta t)$ and $\boldsymbol{r}_i(t-\Delta t)$ leads to:

$$\boldsymbol{r}_i(t+\Delta t) = 2\boldsymbol{r}_i(t) - \boldsymbol{r}_i(t-\Delta t) + \boldsymbol{a}(t)\Delta t^2 + O(\Delta t^4) + \cdots \tag{1.30}$$

where $\boldsymbol{a}_i(t) = -\nabla_i U(\{\boldsymbol{r}_i\})/m_i$ denotes the acceleration. When terms larger than $O(\Delta t^3)$ are neglected one obtains positions that are correct to $O(\Delta t^4)$, whereas velocities are correct to order $O(\Delta t^2)$.

A commonly applied modification is the velocity Verlet algorithm. It explicitly incorporates the particle's velocity, $\boldsymbol{v}_i$, such that:

$$\begin{aligned} \boldsymbol{r}_i(t+\Delta t) &= \boldsymbol{r}_i(t) + \boldsymbol{v}_i(t)\Delta t + \frac{\boldsymbol{a}_i \Delta t^2}{2} \\ \boldsymbol{v}_i(t+\Delta t) &= \boldsymbol{v}_i(t) + \frac{\boldsymbol{a}_i(t) + \boldsymbol{a}_i(t+\Delta t)}{2}\Delta t \end{aligned} \tag{1.31}$$

This approach produces errors that are of the same order as the Verlet algorithm. Its advantage lies in symmetric coordinates for "past" and "future" and conservation of the phase-space volume, that is, the velocity Verlet algorithm is consistent with Liouville's theorem. Although energy is not conserved perfectly on short time scales, there are no energy drifts for large times. The stability of the method can be increased, for example, using "Beeman's algorithm" [128] or the "leap-frog" [129] method, which calculate the velocities more accurately.

In predictor–corrector algorithms time derivatives of the position vectors at time t are used to predict the positions and their derivatives at time $t+\Delta t$. The predicted variables then are corrected according to the difference from those at time t, where a set of "Gear constants" are used. The latter are chosen to balance accuracy and stability, that is, short- and long-time conservation of energy. Optimized values depend on the order of the Taylor expansion ("order of the algorithm").

Predictor–corrector algorithms are only time reversible for $\Delta t \to 0$ and therefore violate Liouville's theorem. However, in the canonical ensemble they can be tuned to be more accurate than the Verlet integration.

The main computational effort in MD simulations is to evaluate the interatomic forces. For pair-wise additive and short-range potentials geometrical composition algorithms have been proposed to optimize the force calculation. Mostly applied are the "cell linked-lists" or the "Verlet list" algorithm. Examples for efficient methods to compute forces from long-range potentials are "Ewald summation" [130], "particle-mesh Ewald" [131], "particle-particle-particle-mesh" [132], and "generalized Born" [133] algorithms.

The MD method has become a powerful tool to simulate even millions of particles and arbitrarily complex molecules in confined systems or in the bulk using periodic boundary conditions. Modifications of the original approach allow for MD simulations at constant pressure, chemical potential, or temperature. "*Ab initio*" MD simulations [134], using first-principles to evaluate interatomic forces for quantum electronic systems, have led to remarkable accomplishments in simulating the properties of real materials.

1.4.2
Non-equilibrium Molecular Dynamics Simulations of Coarse-Grained Polymer Systems

Computational studies of polymeric liquids under non-equilibrium conditions have been performed intensively in recent decades [135–152]. This is not only related to the advancing computational resources that have made such studies possible, but mainly to the distinct advantages of numerical investigations. While experiments usually only provide information on macroscopic properties, non-equilibrium molecular dynamics (NEMD) simulations allow one to explore structural features, which can be related to the phenomenological coefficients that describe the transport of mass, momentum, and energy. NEMD simulations have reproduced successfully many qualitative features of polymer solutions under stationary (steady) shear, such as "shear thinning" (decreasing viscosity with shear rate), "shear alignment" or effects on the normal stress [137, 139–142, 144, 145, 147, 149, 150]. Meanwhile, many numerical studies have been performed even for nonstationary flow fields [140, 145, 146, 150]. However, a reliable characterization of systems out of equilibrium requires careful numerical approaches, where special attention must be paid to coarse-graining, boundary conditions, and thermostat issues. In this section we discuss some of these technical aspects in mesoscopic NEMD simulations for coarse-grained polymer systems.

A presentation that covers the entire field of NEMD simulation techniques would greatly extend the length of this section. Here, we focus mainly on the case of confined polymer systems, where shear deformation is induced by displacement of the confining boundaries. The simulation of bulk systems usually invokes other techniques than discussed here, which are often better suited to reveal homogeneous fluid dynamics. For instance, homogeneous flow fields can be generated by deterministic (e.g., SLLOD [135, 136, 138, 148, 152]) EOM, which have been shown to reveal rather accurate transport properties for atomic liquids [138]. However, complex fluids, such as polymer solutions or melts, tend to "align" under strong shear-deformation due to hydrodynamic instabilities. Homogeneous methods that enforce a linear shear profile therefore have to be applied with care. Simulation methods for atomistic and molecular fluids in homogeneous flow fields have been reviewed in detail [152].

The rigorous solution of the time-dependent, quantum-mechanical, many-body problem is numerically unfeasible. The problem thus must be reduced to classical mechanics and coarse-grained models have to be introduced. In particular for NEMD simulations, the modeling of solvent effects can be crucial and the complexity of the problem is highly dependent on whether the external stimuli are strong or weak and whether they are constant in time or nonstationary.

When hydrodynamic effects are not expected to be important, it is often convenient to simulate without explicit solvent molecules. This approach can still be justified even when hydrodynamic flow becomes relevant, but solvent-related degrees of freedom have to be incorporated on a certain coarse-grained level. To reproduce hydrodynamic effects in the continuum limit, mesoscale hydrodynamic techniques

have been developed that conserve local mass and momentum. Such methods, for example, dissipative particle dynamics [143, 147, 149–151, 153–172], stochastic rotational dynamics [173–181], and the lattice Boltzmann method [182–185], can reproduce hydrodynamic behavior described by the Navier–Stokes equation on the relevant (large) length scales. In these approaches, monomers interact via conservative and thermal forces, where the latter are introduced via a thermostat.

Upon using a thermostat, one assumes that heat transport within the system occurs instantaneously. This is not strictly correct but often it is convenient to simulate at constant temperature. Fluctuation relations are derived more straightforwardly than for the micro-canonical ensemble and the thermostat helps to stabilize particle trajectories, allowing the use of larger time steps. In NEMD simulations, the thermostat is of great importance, as it is used to remove the viscous heat due to the entropy production from external stimuli. However, it is a non-trivial challenge in many NEMD simulations of complex fluids to maintain the temperature and simultaneously avoid an undesired influence of the thermostat on transport properties. For simulations far beyond static equilibrium, the specific choice of the thermostat and its parameters are often crucial. One example, where complications may arise easily, is the shear deformation of confined polymer systems, which is often simulated at shear rates much larger than typical experimental values (see References [142–144]) in order to obtain statistically meaningful results.

Owing to its simplicity, the Langevin (LGV) thermostat is one of the most applied methods to perform simulations in the canonical ensemble. In this approach, the simulated particles are coupled to an external heat bath at constant temperature. The dissipative force acting on particle i is proportional to its velocity:

$$\boldsymbol{F}_i^{\mathrm{d}} = -m_i \Gamma \boldsymbol{v}_i \tag{1.32}$$

where Γ is a friction constant. The random force follows from the fluctuation–dissipation theorem, which defines the temperature of the simulation. The LGV thermostat acts on a local scale. Particles that are too fast are damped by the viscous background, whereas the stochastic heat bath increases the velocity of particles that are too slow. As this method stabilizes the trajectories of monomers very efficiently, the LGV thermostat has been applied for many previous studies [137, 139, 141, 142, 144, 145, 150] of polymeric systems, both in static equilibrium and in NEMD simulations. However, the LGV thermostat does not conserve momentum and screens hydrodynamic interactions beyond a length [170, 186]:

$$\varkappa = \sqrt{\frac{\eta}{\varrho \Gamma}} \tag{1.33}$$

where η and ϱ are viscosity and density, respectively.

Galilean invariance is lost due to the coupling of monomers to the heat bath, which mimics a solvent that rests in the laboratory frame. Therefore, the method belongs to the class of "profile-biased" thermostats [138]. This can be demonstrated easily: Let us consider a film of linear polymers confined by two adsorbing substrates. Shear is applied by moving the upper substrate with a constant velocity, w, while the lower

substrate remains at rest. For a large film thickness, L, the density inhomogeneities close to the substrates are negligible. With η_{bulk} as the bulk viscosity, the Navier–Stokes equation reads [145]:

$$\eta_{\text{bulk}} \Delta \boldsymbol{v}(z) = \Gamma \varrho \boldsymbol{v}(z) \tag{1.34}$$

where z denotes the gradient direction, $\boldsymbol{v}(z)$ is the velocity profile, and ϱ the monomer mass density.

Solving Eq. (1.34) with stick boundary conditions at the lower substrate, $v_x(0) = 0$ (x the shear direction), and assuming $v_x(L) \leq w$ for the upper, leads to [145, 170]:

$$\frac{v_x(z)}{v_x(L)} = \frac{\sinh\left(\sqrt{\Gamma\varrho/\eta_{\text{bulk}}}z\right)}{\sinh\left(\sqrt{\Gamma\varrho/\eta_{\text{bulk}}}L\right)} \tag{1.35}$$

for the monomer velocity profile. The shear stress, σ_{xz}, can be obtained from integrating over the dissipated force [right-hand side of Eq. (1.34)], and for $L \gg \sqrt{\eta_{\text{bulk}}/\Gamma\varrho}$ one finds $\sigma_{xz} \sim \Gamma^{1/2}$. Simulations [145] confirmed this scaling behavior and revealed velocity profiles as given in Eq. (1.35). This outcome obviously is determined by the thermostat, as Eq. (1.34) describes the coupling of monomers to a solvent that remains at rest in the laboratory frame, independent of shear rate [145, 170].

To circumvent a biasing of flow profiles in shear simulations, the LGV thermostat is often applied anisotropically [137, 139, 141, 145, 150]. For instance, the thermostat force may be applied only in gradient and vortex directions, but "deactivated" along the direction of shear. Recent results [150] indicate that, under certain circumstances, a good agreement between this implementation and a method that intrinsically provides Galilean invariance can be achieved (see below). However, the coupling between the shear and gradient directions in complex fluids demands special attention whenever this feature becomes relevant for the transport properties of the confined fluid.

The most straightforward modification of the LGV thermostat is to relate the thermostat forces to the relative velocity of interacting particle pairs. Such an approach is based on the dissipative particle dynamics (DPD) method. Originally, DPD was proposed in conjunction with "soft" interaction potentials, which would represent clusters of atoms, increasing the stability of particle trajectories and allowing the use of larger MD time steps than for "hard" potentials. It has been applied to various problems, for example, phase separation [161, 164, 166], the flow around complex objects [153], and colloidal [154, 162] and polymeric [143, 147, 149–151, 157, 158, 167, 170] systems.

When DPD is applied as a thermostat, dissipative and random forces are added to the total conservative force in a pair-wise form. The sum of thermostat forces acting on a particle pair vanishes such that the microscopic dynamics fulfills Newton's third law. This method provides momentum conservation and Galilean invariance.

At large densities, the DPD thermostat reveals the coupling between the shear and gradient directions and hence is well suited for shear simulations of polymer melts. However, it is important to note that DPD cannot describe hydrodynamic behavior at arbitrary densities when solvent effects are not otherwise incorporated. This affects the applicability of the DPD thermostat already in static equilibrium, where it fails to reproduce Zimm dynamics [189] due to the missing long-range interaction between monomers transmitted by the solvent. To account for hydrodynamic correlations in the dilute regime, solvent effects have to be included on whatever coarse-grained level [143, 147, 157, 165, 167–169, 171], for example, by introducing explicit solvent monomers.

Modified versions of DPD are frequently proposed and the advantages and shortcomings of such modifications are a current issue of research [150, 172, 187]. DPD can be transformed into "smooth-particle hydrodynamics" [188], where the Navier–Stokes equation is solved in a Lagrangian form, or by the application of a splitting algorithm [169] into an Andersen's-thermostat version [165]. The DPD method can also be applied in the micro-canonical ensemble [159, 160, 163]. An extension of DPD has been introduced recently to allow for damping along the parallel and perpendicular components of the relative particle velocities independently [187]. This enables one to tune the transport properties of coarse-grained liquids to better match atomistic NEMD simulations, whenever the latter are feasible. However, the new approach does not conserve local angular momentum and hence should be used with care.

LGV and DPD thermostat have been compared recently [150] for NEMD simulations of polymer brushes. A polymer brush forms when linear polymers are adsorbed on substrates with one chain end, such that the steric repulsions between monomers force the chains to stretch away perpendicularly from the substrate. Systems of two polymer-brush bearing surfaces in contact can sustain large normal loads, simultaneously revealing small friction forces under shear deformation due to shear induced chain inclination. Polymer brushes therefore are very important lubricants and hence are the subject of many NEMD studies [137, 139–142, 144, 145, 147, 151].

For steady-state shear deformation similar transport properties are found at large and intermediate monomer densities, but systematic differences between the two methods arise at small densities. DPD and LGV thermostat also reveal somewhat different results for nonstationary flows [150].

NEMD simulations of polymer brushes at constant shear motion have also been performed with explicit solvent molecules, which are typically introduced as "single monomers." Both the LGV thermostat [139] and DPD [143, 147] exhibit significantly enhanced lubrication properties as compared to simulations of "dry" brushes, revealing the importance of solvent-induced effects on the macroscopic transport coefficients.

Complex polymer systems, such as polymer melts [149, 150] or star polymers [190] embedded between two polymer brushes, have been the subject of recent investigations. Simulations of these systems under nonstationary stimuli are extremely rare.

Alternative approaches to account for hydrodynamic interactions are based on so-called "hybrid" methods, where the polymers are coupled to a dynamical

background. The latter can be introduced either by collisions of ideal-gas particles or by a lattice-based solution of the Boltzmann equation [184], known from the kinetic theory of gases.

The first technique is known as the stochastic rotational dynamics (SRD) method or multiparticle collision dynamics, which is a particle-based algorithm suited to account for hydrodynamic interactions on the mesoscale. The coarse-grained solvent is described as ideal-gas particles that propagate via streaming and collision steps, which are constructed such that the dynamics conserves mass, momentum, and energy.

In the streaming step, the solvent particle trajectories are ballistic. Collisions are introduced by sorting the particles into cubic lattice cells and performing a stochastic rotation of the relative velocities in each cell. In contrast to DPD, the SRD method acts on all particles within the same collision cell.

In SRD, the environment of a particle depends on the superimposed velocity field. This breaks Galilean invariance, because the particles that participate in a collision differ between moving and resting frame. However, when the mean free path length of particles is large compared to the mesh size of the lattice, colliding particles arrive from different cells and are therefore uncorrelated. This reflects the conditions of "molecular chaos," where Galilean invariance is negligible. It has been shown [175] that Galilean invariance can be restored by a randomization of the collision environment, for example, by random shifts of the cells before each collision step.

To simulate polymer solutions, the monomers have to be coupled to the SRD fluid. Different strategies to achieve this aim have been proposed [173, 174, 176–179, 181]. Typically, the EOM of the polymers themselves are integrated with the standard MD method. The monomers are included into the collision step, thereby exchanging momentum with the SRD fluid. This is carried out under conservation of the total momentum. Often it is sufficient to treat the monomers as hydrodynamic point sources and to neglect the excluded volume interaction between solvent and monomers [173]. This method reproduces hydrodynamic behavior on large length scales and therefore reveals Zimm dynamics for dilute linear polymers in static equilibrium [173, 176, 177].

SRD appears to be a very promising (rather new) approach for future NEMD simulations, as it is a very efficient mesoscale technique. It reflects the characteristic shear deformation of solute macromolecules, for example, for shear flows of star polymers [180] or DNA molecules [181].

Hydrodynamic flow also can be incorporated via a discretized version of the Boltzmann equation. This approach is known as the lattice Boltzmann (LB) method. The idea is to solve the linearized Boltzmann equation on an underlying lattice to propagate molecular populations ("fictitious" solvent particles), which define the density and velocity on each lattice site. Similar to SRD, the monomers are treated as hydrodynamic point sources in the continuous space. The flow velocity at the monomer positions follows from a linear interpolation between neighboring lattice sites.

Coupling a stochastic version of LB with standard MD has allowed the reproduction of Zimm dynamics for dilute polymers in static equilibrium [183]. It has been

applied recently to study polymer migration in confined geometries for pressure driven flows [191]. LB also can be used in somewhat different "hybrid" methods [182], where the "point-particle" assumption for the solute is no longer valid, for example, in colloidal systems [185].

The applicability of thermostat implementations and mesoscale hydrodynamic techniques depend strongly on the specific system under consideration and general recommendations in favor of one method cannot be made. However, some guidelines shall be given:

- The LGV thermostat can be ruled out, even in its "profile-unbiased" version, whenever momentum transport is relevant, either in the form of hydrodynamic interactions or, for instance, due to a coupling between the shear and gradient directions. However, the LGV thermostat can be a powerful tool, as it stabilizes the particle trajectories very efficiently and allows the study of systems far from equilibrium. Excellent examples are investigations of polymer brushes at sufficiently large density, where situations far beyond linear response [137, 139, 141, 142, 144, 145, 150] and nonstationary shear deformation [144, 145, 150] could be studied.
- The DPD thermostat is the most straightforward and natural way to introduce Galilean invariance and momentum conservation. Whenever feasible, NEMD simulations with DPD and explicit solvent molecules would yield reasonable mesoscale hydrodynamics. Simulations far beyond static equilibrium [143, 147, 149–151] and nonstationary flows [150] have been performed. However, the level of coarse-graining for the explicit solvent still is a relevant issue.
- The usage of monomers as hydrodynamic point sources coupled to a SRD or LB fluid invokes problems for some systems in NEMD simulations. For instance, shear induced instabilities related to compositional fluctuations at polymer–liquid interfaces cannot be described properly when excluded volume effects are neglected. For nonstationary flow fields, a problem arises matching the time scales of polymer system and background fluid. When adjusted incorrectly, effects stemming from the finite solvent inertia may not be covered.

1.5
Atomistic Simulation of Polymer Melts and Blends Using Molecular Dynamics Techniques

1.5.1
Polymer Melts

Molecular dynamics simulations of polymer melts and blends in full atomistic detail are computationally demanding and a relatively recent approach to complement experimental observations and advance polymer theory [192–201]. The numerical simulation of Newton's equation of motion with suitable interatomic potentials (force fields) for polymers and other common constituents [202, 203] contributes to

understanding of the structural, dynamic, thermal, and mechanical properties of polymer melts. First attempts employed rotational isomeric state models to generate an initial structure and energy minimization (a predecessor method to MD to minimize atomic overlaps), combined with "blowing up" interatomic potentials, to obtain independent static equilibrium models of polymer melts [192]. The system size has since increased from the simulation of a single atactic polypropylene chain in a box of 1.8 nm^3 volume with a few independent configurations to complex polymer systems of 10 nm^3 volume over periods of nanoseconds (millions of time steps of femtoseconds) using desktop computers and over periods of microseconds (billions of time steps of femtoseconds) using supercomputers. The exponentially increasing amount of computational resources opens up new avenues to obtain insight into the dynamics of molten polymers.

In polyisoprene melts, the local polymer dynamics were shown to be independent of initial configurations [193]. Ratios of correlation times for different C–H vectors in the chain backbone match NMR data very well, while absolute values were more than twice as long. The spatial extent of cooperative motion accompanying conformational transitions was found to be about 1–2 repeat units. Diffusion coefficients, friction coefficients, and zero-shear viscosities in models of linear polyethylene melts were computed in very good agreement with experiment [194]. Systems of several chains of length C_{24} to C_{156} were first equilibrated using an efficient end-bridging Monte Carlo algorithm, and then subjected to MD simulation in the NVE and NVT ensembles up to 12 ns. The resulting series of melt properties as a function of chain length significantly expanded the understanding of polymer melts, including radii of gyration and relaxation times. Most importantly, the friction coefficient ξ was found to be constant above a chain length of C_{60}, which is consistent with the Rouse model for an unentangled polymer melt (Figure 1.6).

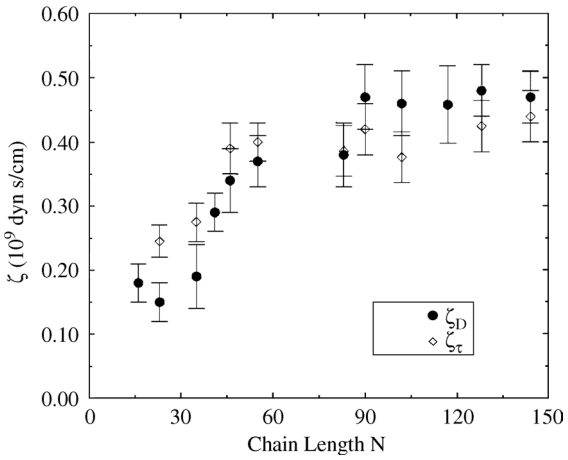

Figure 1.6 Friction coefficient ξ versus chain length N of polyethylene, as obtained from the Rouse relation between ξ and diffusion coefficient D (ξ_D, full symbols) and from the Rouse relation between ξ and the longest relaxation time τ_1 (ξ_τ, open symbols). After Reference [194].

Molecular dynamics methods have been further applied in industrial contexts [195] to gain qualitative insight into viscoelastic properties of polydisperse polymer melts, interface tensions between polymer melts, and the Izod impact strength. Nanoparticles of up to 16 nm diameter composed of chains of length C_{50} to C_{200} of various polymers (PE, PEP, aPP, PIB) were simulated by large-scale parallel MD to estimate glass transition and melting temperatures [196]. According to experiment, the thermal expansion coefficient and the heat capacity increase at the glass transition temperature; both increases were also observed in MD simulation at, however, two distinct temperatures of 50 K below and 50 K above the experimental glass transition. Nevertheless, a qualitative relation between increasing transition temperature and increasing size of the polymer particles has been found. Results obtained so far have been insufficient to demonstrate conclusively the ability to simulate glass transitions reliably and routinely, owing to the long time scales of the transitions and limitations in accuracy of the atomistic models [197, 198]. Several chains of atactic polystyrene of composition $C_{400}H_{402}$ were simulated to investigate the surface structure of thin films [199]. An end-bridging Monte Carlo algorithm was first invoked using a coarse-grained model for equilibration of the melt, followed by mapping onto the full atomistic detail, and molecular dynamics simulation. A preferred orientation of the phenyl rings normal to the surface was found and a surface energy 38 mJ m^{-2} was computed in agreement with experiment. Moreover, dielectric properties of poly (butadiene) [200], glass transitions of various polymers [198], and force field parameters for silamethylene polymers [201] were investigated.

1.5.2 Polymer Blends

The simulation of polymer blends includes mixtures of polymers in the molten and solid states [204–218]. We can distinguish miscible, partially miscible, and immiscible blends as well as mixtures of very specifically interacting biopolymers. For example, direct contacts between residues in a protein (homeodomain of Antennapedia) and DNA bases, as well as the role of water molecules at the interface, have been analyzed during a 2 ns trajectory [204]. Dynamical observations by NMR spectroscopy were consistent with specific interactions derived from the simulation, and the critical role of the Gln-50 residue (pink) for protein–DNA binding, as previously known through genetic and biochemical analysis, could be linked to the interaction with four base pairs and bases in both DNA strands (Figure 1.7). The simulation of similar specific protein–protein interactions [206] and protein–polymer interactions [213] is an interesting extension of the simulation of homopolymers and block-copolymers.

After an efficient initial Monte Carlo equilibration with chain scission and fusion moves, the diffusion of binary liquid blends of *n*-alkanes and polymers was investigated for chain lengths of C_5/C_{78}, C_{10}/C_{78}, and C_{12}/C_{60} using molecular dynamics simulation [207]. Diffusion coefficients of both components increased with increasing weight fraction of the short chain component, which was attributed to the increase in free volume contributed by these solvent-like chains. Results were found

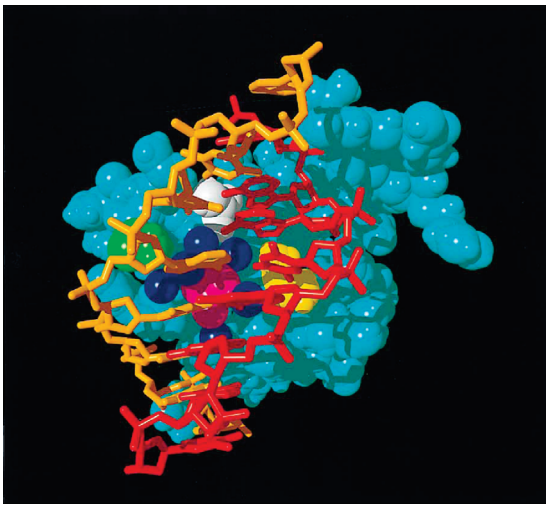

Figure 1.7 Snapshot of a protein–DNA interface (Antennapedia homeodomain–DNA complex). The protein is represented by a space-filling model, with all atoms in cyan except for the side chains of Ile-47 (yellow), Gln-50 (pink), Asn-51 (gray) and Met-54 (green). The DNA is shown as a wireframe model. Positions of interfacial water molecules are given by dark blue spheres. After Reference [204].

to be in good agreement with free volume theory for low and medium fractions of the short alkane, with Rouse theory for all volume fractions, and with measurements of diffusion constants for the C_{12}/C_{60} system across the range of volume fractions and temperatures.

More recently, glass transition temperatures were computed in semi-quantitative agreement with experiment for a cationic polymethacrylate blended with triethyl citrate plasticizer as a function of plasticizer weight content using medium size simulation boxes (3.4 nm^3) in the NPT ensemble (Figure 1.8) [212]. Results of similar quality were also obtained for hydroxyl-terminated poly(butadiene) and poly(glycidyl azide) with various amounts of plasticizers [218]. The findings illustrate the current ability and limitation of all-atom simulations to characterize the phase behavior of polymers and blends as a function of chemistry. The reliability might be further improved through more accurate force fields, particularly with a focus on the precise modeling of polarity [219] and torsion barriers. In addition, stress tensors at interfaces and in arbitrarily shaped volumes within the system can be computed to describe the detailed dynamic mechanical behavior, including additive contributions from bonded, Coulomb, and van der Waals interactions to the total stress [220]. Notably, however, the quantitative prediction of glass transition temperatures meets the principal problem that the structural relaxation time of the polymer melt slows down dramatically in the temperature region slightly above the glass transition, where it reaches typically about 1 s. Molecular dynamics studies can equilibrate atomistic models of polymer melts often only on the nanosecond timescale, and hence one observes that the polymer melt falls out of equilibrium already at

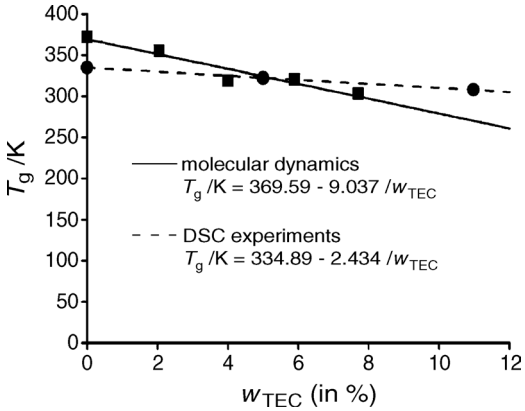

Figure 1.8 Dependence of the glass transition temperature T_g of a cationic polymethacrylate on the weight proportion of plasticizer w_{TEC}. A comparison of experimental values from DSC (dashed line) and computed values from all-atom simulation (full line) is shown. After Reference [212].

temperatures clearly above the glass transition temperature. This effect has been demonstrated by variation of the cooling rate for coarse-grained models [221]. Therefore, one would expect that normally the glass transition temperature found in simulations is an overestimate (the absolute difference is largest for the so-called "strong glassformers" and weakest for the so-called "fragile glassformers"). In view of this fact, the good agreement between experimental results and simulations sometimes reported in the literature is somewhat surprising. Partially, this may be due to a lucky cancellation of errors (the potentials used in the modeling may not always be very accurate, and if they underestimate the real glass transition temperature this may partially offset the systematic shift to higher temperatures due to the too short observation times in the simulation). In any case, more systematic studies will be needed to clearly resolve these problems.

Several studies also underline the importance of very efficient equilibration algorithms and long trajectories to understand the miscibility of long polymer chains in blends and at interfaces. Using relatively short MD trajectories without a significant equilibration algorithm, computed surface and interface tensions of various thin film interfaces of polyethylene, polypropylene, poly(ethylpropylene), and short copolymers of chain length C_{200} lead to uncertainties in excess of $20\,\mathrm{mJ\,m^{-2}}$ [205]. In comparison, computed surface and interface tensions of shorter surfactants, such as attached to inorganic filler components, lead to uncertainties of only $2\,\mathrm{mJ\,m^{-2}}$ [222]. Similarly, MD simulations of a poly(vinylphenol)/poly(vinyl methyl ether) blend with long chains of $N = 250$ for each polymer without a significant equilibration algorithm did not result in uniform mixing [209]. Nevertheless, local structural correlations such as the gauche-to-anti ratio and the formation of hydrogen bonds can be understood, as further demonstrated for poly (vinylphenol)/poly(ethylene terephthalate) [210] and polystyrene/polyisoprene blends [211]. As discussed in the introduction, the standard elementary description of miscibility in polymer blends uses the concept of the "Flory–Huggins

χ-parameter" and for large molecular weights (degree of polymerization of the order of 1000 or more) partial miscibility occurs only if χ is rather small, of the order of 1 part in a thousand. Such small values need an almost perfect compensation between effective interactions of like and unlike monomeric units (taking also the steric arrangements of these units in the blend into account). Although it would be very desirable to be able to predict these χ-parameters accurately from simulation, one cannot yet expect that the models are accurate enough for this purpose in the general case. In addition, polymer blends are characterized by spatial correlations on rather large scales and slow relaxation of concentration fluctuations, and therefore, so far, many studies have relied on coarse-grained models exclusively [9]. Going beyond such coarse-grained descriptions clearly is desirable, of course, and the mapping between coarse-grained and atomistic models, discussed in the next subsection, is a promising direction towards this goal.

Further results of all-atom molecular dynamics simulations have also been reported for PEO/PMMA blends [214], POSS/PE blends [215], blends of hydroxyl-terminated polybutadiene with explosive plasticizers [217], as well as a novel force field for PDMS and mixtures with alkanes [216]. The simulation of multiphase polymer systems has also been reviewed [208].

1.5.3
Reversible Mapping between Atomistic, Coarse Grained, and Field Models

Understanding the complex phase properties of polymer blends benefits from simulation methods at different length scales, and efforts to achieve compatibility and convertibility between these length scales have been made [223–227]. A common approach involves the iterative match of radial distribution functions from atomistic simulations of an oligomer to those calculated in a coarse-grained simulation for the same oligomer (Figure 1.9) [223]. Similarly, coarse-grained models representing an oligomer of few repeat units in one bead can be mapped to yet coarser models representing many repeat units in one bead to simulate high polymers. In addition, to match structural information such as radial distribution functions, a match of free energies such as surface tensions and solubility parameters is required. The difference in length and time scales also necessitates suitable scale factors to interpret distance and time consistently at both scales. The neglect of numerous degrees of freedom from the atomistic to the coarse-grained scale makes it difficult to compare

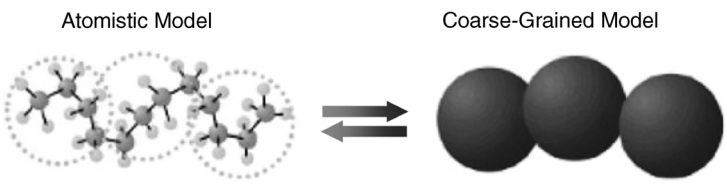

Figure 1.9 Conversion between atomistic and coarse-grained models. A 4 : 1 coarse-graining scheme is shown. After Reference[226].

time scales more accurately than within an order of magnitude [224]. First estimates for an appropriate scale factor and dynamic mapping approaches can be derived from a comparison of computed diffusion constants at both scales and the conversion of Lennard-Jones (reduced) time in the coarse-grained simulation into real time.

The efficiency of a reversible mapping approach also depends on a well-defined (or even automatic) parametrization method such as the simplex method or iterative Boltzmann inversion [223]. A useful route to relaxed high polymer structures can be (i) an atomistic simulation, (ii) the derivation of a coarse-grained model, (iii) a coarse-grained simulation using suitable algorithms, (iv) reverse mapping to the atomistic level, and (v) local relaxation of the atomistic structure (Figure 1.9). For example, iterative Boltzmann inversion has been applied to study the phase separation in a polystyrene/polyisoprene blend and leads to qualitative agreement with experiment [225].

Further methods to study mesoscopic structures include time dependent Ginzburg–Landau theory, dynamic density functional theory, lattice-gas automata, and the lattice Boltzmann equation [226]. Some of these simulation methods, such as the dynamic mean field theory (Mesodyn) and dissipative particle dynamics (DPD), utilize coarse-grained molecular models to study the morphology of inhomogeneous materials using Flory–Huggins χ parameters between components and can be reversibly linked to atomistic simulation. For example, Flory–Huggins χ parameters between two components, characteristic ratios (C_∞) of the Gaussian chains, and self-diffusion coefficients (D) have been estimated through atomistic simulation and fed into coarse-grained models in the mesoscopic simulation [226]. Trends in thermodynamically preferred morphology, phase separation, mechanical properties, and the behavior under shear were obtained in good agreement with experiment for various polymer blends, including polyethylene/polypropylene, poly(ethylene terephthalate)/poly(ethylene naphthalate), poly(vinyl chloride)/polyethylene, poly (methyl methacrylate)/polycarbonate, and polycarbonate/acrylonitrile/butadiene/styrene [226], as well as composites [227]. The mesoscale morphologies and structures can be converted into atomistic models for continued analysis at a chemically specific level.

1.5.4
Comparison to Experiment and Future Challenges

The previous sections indicate the ability of chemically detailed simulations to explain experimental data and the potential for predictions in unknown systems. All-atomic simulation often bridges the gap between indirect structural information obtained from spectroscopic, thermal, and mechanical measurements and molecular level details. The local dynamics of polymer chains [193] agrees with C-H NMR relaxation data on a relative scale [2]; however, absolute correlation times in the simulation appear to be $\sim$2.5 times the real value. This mismatch could be associated with overestimated torsion barriers in atomistic models, such as an eclipsed barrier of 5–6 kcal mol^{-1} for *n*-butane (from *ab initio* calculations) in comparison to the experimental value of 4.0 kcal mol^{-1} [228]; such differences can

be corrected in future force fields. Nevertheless, diffusion coefficients, friction coefficients, and zero-shear viscosities have been computed in very good agreement with experiment [194], and model predictions both at the atomistic and coarse-grained level can be considered reliable over significant temperature and pressure ranges for non-polar polymers such as polyethylene, polypropylene, or polyisobutylene. The availability of high-performance computing resources [195, 196, 199] further aids in obtaining equilibrium structures and in the application of new equilibration algorithms for large systems.

In polar polymers, the exact balance of charges and the description of specific interactions such as hydrogen bonds are critical [219]. Often, X-ray diffraction data, NMR data, and binding constants are valuable experimental input to identify specific van der Waals, π-stacking, and polar interactions on the basis of molecular simulation [204]. Therefore, atomic-level simulations have great potential in the design of complex interfaces or "mixtures" of biological and bioinspired polymers in combination with experiment. Properties such as gas diffusion constants, elastic constants, and possibly glass transition temperatures as well as solubility parameters could be simulated in approximate agreement with experiment, as recently shown for chitosan [229]. Self-diffusion coefficients for short-chain polymer blends have been obtained in quantitative agreement with experiment [207], and current limitations on chain length (10^2–10^3 main chain atoms) will be pushed back as computational power becomes more readily available. In the same way, it is likely that surface and interface properties in polymer blends will be computed quantitatively in the near future. In addition to the previously mentioned techniques, electron paramagnetic resonance spectroscopy (EPR) also constitutes a helpful tool in combination with all-atom simulations to monitor the dynamics in spin-probe labeled polymers at a length scale of 1–10 nm, which is of interest in chain dynamics [230]. Ultimately, the phase behavior and mechanical properties of long-chain polymer blends can be most effectively simulated through multiscale approaches, for example, coarse-grained models and field-based descriptions, which can be parameterized on the basis of atomistic models and converted from the atomistic into the simplified scale as well as vice versa.

1.6 Concluding Remarks

The subject of molecular simulation and thermodynamics of polymers is an active area of research and encouraging results have been obtained. The interplay between the refinement of computer simulation methods and the rapid growth of computer resources (the speed of the hardware is doubling roughly about every two years) has led to a rapid growth of successful applications of simulation methods.

While for the first 30 years after the introduction (in 1941) of the Flory–Huggins theory of polymer blends (and polymer solutions) experimentalists had to exclusively rely on this approach and its refinements for the interpretation of their data, in the two decades from about 1970 to about 1990 basic steps were taken to go beyond this phenomenological description, both via the formulation of more detailed and refined

theories [e.g., the self-consistent field theory (SCFT) of polymeric systems, the statistical associating fluid theory (SAFT) for the description of the equation of state, and the polymer reference interaction site model (PRISM), etc.] and via computer simulation methods. Owing to lack of computer resources, the first successful applications focused on Monte Carlo simulations of lattice models (such as self-avoiding walks on the simple cubic lattice, or the bond fluctuation model), providing crucial tests of the Flory–Huggins theory of polymer mixtures, elucidating their limitations, and of the random phase approximation applied to polymer blends and block copolymers, and so on. Alternative coarse-grained off-lattice models such as the Kremer–Grest bead-spring model were also introduced, offering the important advantage that via molecular dynamics simulations dynamical aspects of polymer blends, melts, and solutions also became accessible (interdiffusion and spinodal decomposition in blends and solutions; selfdiffusion in melts and the entanglement problem; glass transition in polymeric systems).

Of course, while work along such lines can elucidate basic theoretical questions, provide general insight into the problems, and give guidance to experiments, the important task of predicting properties of polymeric materials from "first principles" (i.e., only the knowledge of chemical structure is used as the input) cannot be addressed using such coarse-grained models alone. It must also be stressed that a theoretically fully satisfactory treatment would require us to solve the many-body Schrödinger equation for all the electrons plus nuclei in the system and use the resulting energy eigenvalues and associated eigenfunctions in a quantum statistical mechanics framework; unfortunately, such an approach is still far from feasible. Consequently, all simulations of "chemically realistic" models rely on approximate descriptions, which again need to be validated by comparison to experiment. In fact, for polymeric materials, in most cases effects due to electrons are not explicitly considered, and one uses effective potentials ("force fields") as input in molecular dynamics simulations (which amount to the solution of Newton's equations of motion, i.e., classical mechanics rather than quantum mechanics). While some parts of such potentials (e.g., torsional potentials) can be derived from presumably very reliable quantum chemistry approaches, the non-bonded dispersion forces cannot be deduced reliably from any "first principles"-theories. Thus, both coarse-grained and atomistic models describe the latter often by the phenomenological Lennard-Jones potential, with parameters chosen such that the model correctly reproduces selected experimental data in a simulation. Of course, great care is necessary so that in such applications the "technical" limitations of simulations (polymeric systems often involve large length scales and hence one needs to watch out for finite size effects; polymeric systems often involve huge relaxation times, and hence the question of whether equilibrium has been reached needs to be addressed) are adequately considered. As a general rule, we stress that sound simulation work needs a careful "education" of the simulator in the techniques that he or she is using, and in their theoretical background; the present chapter could only give the flavor of this background, and has hopefully "whetted the appetite" of the reader to study this background more thoroughly. Any would-be practitioner of such techniques must realize that it would be completely wrong and misleading to think that simulation

methods are already a standard tool that everybody can use without prior knowledge, just as experimentalists can use standard instruments (microscopes, light or X-ray scattering apparatus, etc.). The idea that computer simulation belongs to this category of "standard tools" is clearly a vision but not yet reality.

Owing to the problem that one needs to connect quantum-mechanical input (sub-ångström length scale, sub-picosecond time scale) to the scales of coarse-grained models (many nanometers and many nanoseconds) and the latter to the mesoscopic scales of interest for many problems (many micrometers or even millimeters and time scales up to seconds are the length- and time-scales of interest for the processing of real polymeric materials), it is clear that a straightforward brute-force approach (if ever feasible at all) is not the most economical approach to the problem. Hence the idea of a hierarchical "multiscale modeling" approach is clearly attractive and the first promising steps in this direction can be found in the literature. In the present chapter we have, hence, illustrated this very interesting development. However, we also emphasize that at present this is still a very active area of research, and universally applicable methods (including also an understanding of the accuracy of the approach under various circumstances) have yet to emerge.

Symbols

$<>_T$	thermal average
A	Hamaker constant or Helmholtz free energy
$\boldsymbol{a}_i$	acceleration (molecular dynamics)
a_{ij}	probability of selecting or placing a particular particle for the move (Monte Carlo)
b	statistical segment length
$c_i^{\mathrm{A,B}}$	local concentrations (Flory–Huggins model)
C_∞	characteristic ratio
D	self-diffusion coefficient
F_i	force acting on particle i
$H(n)$	number of occurrence in state n (successive umbrella sampling)
F	Helmholtz free energy
k_B	Boltzmann constant
L	linear box size
m_i	mass of particle i
M	order parameter
n	number of particles
$N_{\mathrm{A,B}}$	chain length of polymer type A or B (Flory–Huggins model)
p	pressure
$P(i)$	probability of residing in state in state i (Monte Carlo)
P_{sim}	simulated probability (multicanonical sampling)
q	number of nearest neighbors (Flory–Huggins model)
R_g	radius of gyration
$\boldsymbol{r}_i$	position of particle

T	temperature
T_c	critical temperature
U	potential
U_2	second-order cumulant
U_4	fourth-order cumulant
V	volume
V_{FENE}	FENE potential
$\boldsymbol{v}_i$	velocity of particle i
$V_{LJ}(r)$	Lennard-Jones potential
$w(n)$	weight function (multicanonical sampling)
Z	partition sum

Greek Symbols

$\beta = 1/k_B T$	
γ	interfacial tension
Γ	friction constant
$\varepsilon_{AA}, \varepsilon_{AB}$ *and* ε_{BB}	interaction energies (Flory–Huggins model)
ε, σ	interaction parameters in Lennard-Jones model
η	viscosity
Θ	contact angle
μ	chemical potential
ξ	friction coefficient or empirical modification parameter in Lorentz–Berthelot rule or correlation length
ϱ	density
σ_{xz}	shear stress
φ_A, φ_B *and* φ_V	volume fractions (Flory–Huggins model)
χ_{AB}, χ_{AA} *and* χ_{BB}	Flory–Huggins parameters
ω_{ij}	probability of jumping from state i to j (Monte Carlo simulation)
Ω	grand canonical potential

References

1 Huggins, M.J. (1941) *J. Chem. Phys.*, **9**, 440; Flory, P.-J. (1941) *J. Chem. Phys.*, **9**, 660.
2 Flory, P.-J. (1953) *Principles of Polymer Chemistry*, Cornell University Press, Ithaca, N.Y.
3 de Gennes, P.G. (1979) *Scaling Concepts in Polymer Physics*, Cornell University Press, Ithaca, N.Y.
4 Binder, K. (1994) *Adv. Polym. Sci.*, **112**, 181.
5 Koningsveld, R., Stockmayer, W.-H., and Nies, E. (2001) *Polymer Phase Diagrams*, Oxford University Press, Oxford.
6 Rubinstein, M. and Colby, R.H. (2003) *Polymers Physics*, Oxford University Press, Oxford.
7 Binder, K., Müller, M., Virnau, P., and MacDowell, L.G. (2005) *Adv. Polym. Sci.*, **173**, 1.
8 Bicerano, J. (ed.) (1992) *Computational Modeling of Polymers*, Marcel Dekker, New York.
9 Binder, K. (ed.) (1995) *Monte Carlo and Molecular Dynamics Simulations in Polymer Science*, Oxford University Press, New York.

10 Kotelanskii, M. and Theodorou, D.N. (eds) (2004) *Simulation Methods for Polymers*, Marcel Dekker, New York.

11 Sariban, A. and Binder, K. (1987) *J. Chem. Phys.*, **86**, 5859; Sariban, A. and Binder, K. (1988) *Macromolecules*, **21**, 711.

12 Binder, K.,in (1995) *Monte Carlo and Molecular Dynamics Simulations in Polymer Science* (ed. K. Binder), Oxford University Press, New York, p. 356.

13 Müller, M. (1995) *Macromolecules*, **28**, 1825; Müller, M. (1999) *Macromol. Theory Simul.*, **8**, 343.

14 Kemmere, M.F. and Meyer, Th. (eds) (2005) *Supercritical Carbon Dioxide in Polymer Reaction Engineering*, Wiley-VCH Verlag GmbH, Weinheim.

15 Deutsch, H.-P. and Binder, K. (1992) *Macromolecules*, **25**, 6214; Deutsch, H.-P. and Binder, K. (1993) *J. Phys. (Paris) II*, **3**, 1049.

16 Bates, F.S., Rosedale, J.H., Stepanek, P., Lodge, T.P., Fredrickson, G.H., and Helm, P.P. Jr (1990) *Phys. Rev. Lett.*, **65**, 1893; Stepanek, P., Lodge, T.P., Kredowski, C., and Bates, F.S. (1991) *J. Chem. Phys.*, **94**, 8289.

17 Meier, G., Schwahn, D., Mortensen, K., and Janssen, S. (1993) *Europhys. Lett.*, **22**, 577; Schwahn, D., Meier, H., Mortensen, K., and Janssen, S. (1994) *J. Phys. II (Paris)*, **4**, 837.

18 Schwahn, D. (2005) *Adv. Polym. Sci.*, **183**, 1.

19 Melnichenko, Y.B., Anisimov, M.A., Povodyrev, A.A., Wignall, G.D., Sengers, J.V., and Van Hook, W.A. (1977) *Phys. Rev. Lett.*, **79**, 5266.

20 Sanchez, I.C. and Lacombe, R.H. (1976) *J. Phys. Chem.*, **80**, 2352; Lacombe, R.H., and Sanchez, I.C. (1978) *Macromolecules*, **11**, 1145.

21 Bawendi, M.G. and Freed, K.F. (1988) *J. Chem. Phys.*, **88**, 2741; Freed, K.F. and Bawendi, M.G. (1989) *J. Phys. Chem.*, **93**, 2194.

22 Dudowicz, J., Freed, K.F., and Madden, W.-G. (1990) *Macromolecules*, **23**, 4803; Dudowicz, J. and Freed, K.F. (1991) *Macromolecules*, **24**, 5076–5112.

23 Freed, K.F. and Dudowicz, J. (1995) *Trends Polym. Sci.*, **3**, 248; Freed, K.F. and Dudowicz, J. (1998) *Macromolecules*, **31**, 6681; Freed, K.F. and Dudowicz, J. (2005) *Adv. Polym. Sci.*, **183**, 63; Dudowicz, J. and Freed, K.F. (1995) *Macromolecules*, **28**, 6625; Dudowicz, J. and Freed, K.F. (1996) *Macromolecules*, **29**, 8960; Foreman, K.W. and Freed, K.F. (1998) *Adv. Chem. Phys.*, **103**, 335.

24 Edwards, S.F. (1965) *Proc. Phys. Soc. London*, **85**, 613.

25 Doi, M. and Edwards, S.F. (1986) *Theory of Polymer Dynamics*, Academic Press, New York.

26 Grosberg, A.Yu. and Khokhlov, A.R. (1994) *Statistical Physics of Macromolecules*, AIP, New York,Helfand, E. and Tagami, Y. (1971) *J. Polym. Sci., Part B, Polym. Lett.*, **9**, 741.

27 Helfand, E. (1975) *J. Chem. Phys.*, **62**, 999.

28 Scheutjens, J.M.H.M. and Fleer, G.J. (1973) *J. Phys. Chem.*, **83**, 1619.

29 Hong, K.M. and Noolandi, J. (1981) *Macromolecules*, **14**, 727; Noolandi, J. and Hong, K.M. (1983) *Macromolecules*, **15**, 483; 1983, **16**, 1443; Whitemore, D.M. and Noolandi, J. (1985) *Macromolecules*, **18**, 657; Whitemore, D.M. and Noolandi, J. (1995) *Macromoleclues*, **28**, 5763.

30 Matsen, M.W. (1995) *Macromolecules*, **28**, 5763; Matsen, M.W. (1999) *J. Chem. Phys.*, **110**, 4658.

31 Müller, M. and MacDowell, L.G. (2003) *J. Phys.: Condens. Matter*, **15**, R609.

32 Fredrickson, G.H. (2006) *The Equilibrium Theory of Inhomogeneous Polymers*, Oxford University Press, New York.

33 Hamley, I.W. (1998) *The Physics of Block Copolymers*, Oxford University Press, Oxford.

34 Schweizer, K.S. and Curro, J.G. (1987) *Phys. Rev. Lett.*, **58**, 246; Schweizer, K.S. and Curro, J.G. (1988) *Phys. Rev. Lett.*, **60**, 809; Schweizer, K.S. and Curro, J.G. (1988) *J. Chem. Phys.*, **88**, 7242; Schweizer, K.S. and Curro, J.G. (1989) *J. Chem. Phys.*, **91**, 5059.

35 Curro, J.G. and Schweizer, K.S. (1990) *Macromolecules*, **23**, 1402; Curro, J.G. and Schweizer, K.S. (1991) *Macromolecules*, **24**, 6736; Curro, J.G., Schweizer, K.S., Grest, G.S., and Kremer, K. (1989) *J. Chem. Phys.*, **91**, 1357.

36 Yethiraj, A. and Schweizer, K.S. (1992) *J. Chem. Phys.*, **97**, 5927; Yethiraj, A. and

Schweizer, K.S. (1993) *J. Chem. Phys.*, **98**, 9080; Schweizer, K.S. and Yethiraj, A. (1993) *J. Chem. Phys.*, **98**, 9053; Yethiraj, A. (1995) *J. Chem. Phys.*, **102**, 6874.
37 Schweizer, K.S. and Curro, J.G. (1994) *Adv. Polym. Sci.*, **116**, 319.
38 Schweizer, K.S. and Curro, J.G. (1997) *Adv. Chem. Phys.*, **98**, 1.
39 Fuchs, M. and Schweizer, K.S. (2000) *Europhys. Lett.*, **51**, 621; Fuchs, M. and Schweizer, K.S. (2001) *Phys. Rev. E*, **64**, 021514.
40 Fuchs, M. and Schweizer, K.S. (2002) *J. Phys.: Condens. Matter*, **14**, R239.
41 Lipson, J.E.G. (1991) *Macromolecules*, **24**, 1334; Lipson, J.E.G. (1992) *J. Chem. Phys.*, **96**, 1418; Sevian, H.M., Brazhink, P.K., and Lipson, J.E.G. (1993) *J. Chem. Phys.*, **99**, 4112.
42 Taylor, M.P. and Lipson, J.E.G. (1998) *J. Chem. Phys.*, **102**, 2118.
43 Dickman, R. and Hall, C.K. (1986) *J. Chem. Phys.*, **85**, 4108; Honnell, K.G. and Hall, C.K. (1989) *J. Chem. Phys.*, **90**, 1841; Yethiraj, A. and Hall, C.K. (1991) *J. Chem. Phys.*, **95**, 8494.
44 Costa, L.A., Zhou, Y., Hall, C.K., and Carra, S. (1995) *J. Chem. Phys.*, **102**, 6212.
45 Wertheim, M.S. (1984) *J. Stat. Phys.*, **35**, 19; Wertheim, M.S. (1984) *J. Stat. Phys.*, **35**, Wertheim, M.S. (1986) *J. Stat. Phys.*, **42**, 459; Wertheim, M.S. (1986) *J. Stat. Phys.*, **42**, 477.
46 Wertheim, M.S. (1986) *J. Chem. Phys.*, **85**, 2929; Wertheim, M.S. (1987) *J. Chem. Phys.*, **87**, 7323.
47 Virnau, P., Müller, M., MacDowell, L.G., and Binder, K. (2004) *J. Chem. Phys.*, **121**, 2169.
48 Mognetti, B.M., Virnau, P., Yelash, L., Paul, W., Binder, K., Müller, M., and MacDowell, L.G. (2009) *J. Chem. Phys.*, **130**, 044101.
49 MacDowell, L.G., Müller, M., Vega, C., and Binder, K. (2000) *J. Chem. Phys.*, **113**, 419.
50 MacDowell, L.G., Virnau, P., Müller, M., and Binder, K. (2002) *J. Chem. Phys.*, **117**, 6360.
51 Hansen, J.P. and McDonald, I.R. (1986) *Theory of Simple Liquids*, Academic, New York.
52 Chapman, W.G., Gubbins, K.E., Jackson, G., and Radosz, M. (1989) *Fluid Phase Equilib.*, **52**, 31; Chapman, W.G., Gubbins, K.E., Jackson, G., and Radosz, M. (1990) *Ind. Eng. Chem. Res.*, **29**, 1709.
53 Blas, F.J. and Vega, L.F. (1997) *Mol. Phys.*, **92**, 135; Blas, F.J. and Vega, L.F. (1998) *Ind. Eng. Chem. Res.*, **37**, 660.
54 Müller, E.A. and Gubbins, K.E. (2001) *Ind. Eng. Chem. Res.*, **40**, 2198.
55 Economou, L.G. (2002) *Ind. Eng. Chem. Res.*, **41**, 953.
56 Gross, J. and Sadowski, G. (2001) *Ind. Eng. Chem. Res.*, **40**, 1244; Gross, J. and Sadowski, G. (2002) *Ind. Eng. Chem. Res.*, **41**, 1084.
57 Barker, J.A. and Henderson, D. (1967) *J. Chem. Phys.*, **47**, 4714.
58 Yelash, L., Müller, M., Paul, W., and Binder, K. (2005) *J. Chem. Phys.*, **123**, 014908.
59 Yelash, L., Müller, M., Paul, W., and Binder, K. (2005) *Phys. Chem. Chem. Phys.*, **7**, 3728.
60 Binder, K. (ed.) (1979) *Monte Carlo Methods in Statistical Physics*, Springer, Berlin.
61 Binder, K. and Cicotti, G. (eds). (1996) *Monte Carlo and Simulations of Condensed Matter*, Societa Italiana di Fisica, Bologna.
62 Frenkel, D. and Smit, B. (2002) *Understanding Molecular Simulation: From Algorithms to Applications*, 2nd edn, Academic Press, San Diego.
63 Landau, D.P. and Binder, K. (2005) *A Guide to Monte Carlo Simulations in Statistical Physics*, 2nd edn, Cambridge University Press, Cambridge.
64 Ferrario, M., Ciccotti, G. and Binder, K. (eds) (2006) *Computer Simulations in Condensed Matter: From Materials to Chemical Biology*, vols 1, 2, Springer, Berlin.
65 Orr, W.J.C. (1947) *Trans. Faraday Soc.*, **43**, 12.
66 Montroll, E.W. (1950) *J. Chem. Phys.*, **18**, 734.
67 Dill, K.A. (1985) *Biochemistry*, **24**, 1501.
68 Baschnagel, J., Wittmer, J., and Meyer, H. (2004) *NIC Ser.*, **23**, 83.
69 Carmesin, I. and Kremer, K. (1988) *Macromolecules*, **21**, 2819.
70 Grest, G.S. and Kremer, K. (1986) *Phys. Rev. A*, **33**, 3628.

71 Kremer, K. and Grest, G.S. (1990) *J. Chem. Phys.*, **92**, 5057.

72 MacKerell, A.D., Banavali, N., and Foloppe, N. (2001) *Biopolymers*, **56**, 257.

73 Kron, A.K. (1965) *Polym. Sci. U.S.S.R.*, **7**, 1361.

74 Wall, F.T. and Mandel, F. (1975) *J. Chem. Phys.*, **63**, 4592.

75 Madras, N. and Sokal, A. (1998) *J. Stat. Phys.*, **50**, 109.

76 Kennedy, T. (2002) *J. Stat. Phys.*, **106**, 407.

77 Mansfield, M.L. (1982) *J. Chem. Phys.*, **77**, 1554.

78 Deutsch, J.M. (1997) *J. Chem. Phys.*, **106**, 8849.

79 Reith, D., Virnau, P. (2010) *Comput. Phys. Commun.* **181**, 800.

80 Karayiannis, N.C., Mavrantzas, V.G., and Theodorou, D.N. (2002) *Phys. Rev. Lett.*, **88**, 105503.

81 Cavallo, A., Müller, M., and Binder, K. (2003) *Europhys. Lett.*, **61**, 214.

82 Mognetti, B.M., Virnau, P., Yelash, L., Paul, W., Binder, K., Müller, M., and MacDowell, L.G. (2008) *J. Chem. Phys.*, **128**, 104501.

83 Panagiotopoulos, A.Z. (1987) *Mol. Phys.*, **61**, 813.

84 Metropolis, N., Rosenbluth, A.W., Rosenbluth, M.N., Telleri, A.H., and Teller, E. (1953) *J. Chem. Phys.*, **21**, 1087.

85 Harris, J. and Rice, S.A. (1988) *J. Chem. Phys.*, **88**, 1298.

86 Frenkel, D., Mooij, G.C.A.M., and Smit, B. (1992) *J. Phys. Condens. Matter*, **4**, 3053.

87 Siepmann, J.I. and Frenkel, D. (1992) *Mol. Phys*, **75**, 59.

88 de Pablo, J.J., Laso, M., and Suter, U.W. (1992) *J. Chem. Phys.*, **96**, 2395.

89 Binder, K. and Landau, D. (1984) *Phys. Rev. B*, **30**, 1477.

90 Borgs, C. and Kotecky, R. (1990) *J. Stat. Phys.*, **60**, 79.

91 Ferrenberg, A.M. and Swendsen, R.H. (1988) *Phys. Rev. Lett.*, **61**, 2635.

92 Wilding, N.B. and Bruce, A.D. (1992) *J. Phys. Condens. Matter*, **4**, 3087–3108.

93 Lee-Koo, M. and Green, M.S. (1981) *Phys. Rev. A*, **23**, 2650.

94 Binder, K. (1981) *Z. Phys. B*, **43**, 119.

95 Privman, V. (ed.) (1990) *Finite-Size Scaling Theory Finite Size Scaling and Numerical Simulation of Statistical Systems*, World Scientific, p. 1.

96 Barber, M.E., Domb, C. and Lebowitz, J.L. (eds) (1983) *Finite-Size Scaling Phase Transitions and Critical Phenomena*, vol. **8**, Academic Press, p. 146.

97 Fisher, M.E. and Green, M.S. (eds) (1971) *Critical Phenomena*, Academic Press, London, p. 1.

98 Berg, B.A. and Neuhaus, T. (1992) *Phys. Rev. Lett.*, **68**, 9.

99 Wang, F. and Landau, D.P. (2001) *Phys. Rev. Lett.*, **86**, 2050.

100 Wang, F. and Landau, D.P. (2001) *Phys. Rev. E*, **64**, 056101.

101 Yan, Q. and de Pablo, J.J. (2003) *Phys. Rev. Lett.*, **90**, 035701.

102 Hansmann, U.H.E. and Wille, L.T. (2002) *Phys. Rev. Lett.*, **88**, 068105.

103 Binder, K. and Heermann, D.W., 4th ed. (2002) *Monte Carlo Simulations in Statistical Physics: An Introduction*, Springer, Berlin.

104 Torrie, G.M. and Valleau, J.P. (1977) *J. Comput. Phys.*, **23**, 187.

105 Virnau, P. and Müller, M. (2004) *J. Chem. Phys.*, **120**, 10925.

106 Binder, K. (1982) *Phys. Rev. A*, **25**, 1699.

107 Grossmann, B. and Laursen, M.L. (1993) *Nucl. Phys. B*, **408**, 637.

108 Müller, M. and Schick, M. (1996) *J. Chem. Phys.*, **105**, 8885.

109 Schneider, G., Alwani, Z., Heim, W., Horvath, E., and Franck, E.U. (1967) *Chem.-Ing.-Tech.*, **39**, 649.

110 Charoensombut-Amon, T., Martin, R.J., and Kobayashi, R. (1986) *Fluid Phase Equilib.*, **31**, 89.

111 Mognetti, M., Oettel, M., Yelash, L., Virnau, P., Paul, W., and Binder, K. (2008) *Phys. Rev. E*, **77**, 041506.

112 Binder, K., Landau, D.P., and Müller, M. (2003) *J. Stat. Phys.*, **110**, 1411.

113 Metzger, S., Müller, M., Binder, K., and Baschnagel, J. (2003) *J. Chem. Phys.*, **118**, 8489.

114 Schick, M. (1990) *Liquids at Interfaces*, (eds J. Charvolin, J.F. Joanny, and J. Zinn-Justin) Elsevier Science Publishers B.V., Amsterdam, p. 415.

115 Eisenriegler, E., Kremer, K., and Binder, K. (1982) *J. Chem. Phys.*, **77**, 6296.

116 Metzger, S., Müller, M., Binder, K., and Baschnagel, J. (2002) *Macromol. Theory Simul.*, **11**, 985.

117 Descas, R., Sommer, J.U., and Blumen, A. (2004) *J. Chem. Phys.*, **120**, 8831.

118 delle Site, L., Abrams, C.F., Alavi, A., and Kremer, K. (2002) *Phys. Rev. Lett.*, **89**, 156103.

119 Young, T. (1805) *Philos. Trans. R. Soc. London*, **5**, 65.

120 Müller, M. and MacDowell, L.G. (2000) *Macromolecules*, **33**, 3902.

121 MacDowell, L.G., Müller, M., and Binder, K. (2002) *Colloids Surf., A*, **206**, 277.

122 MacDowell, L.G., Virnau, P., Müller, M., and Binder, K. (2004) *J. Chem. Phys.*, **120**, 5293.

123 Servantie, J. and Müller, M. (2008) *J. Chem. Phys.*, **128**, 014709.

124 Müller, M. and Binder, K. (1998) *Macromolecules*, **31**, 8323.

125 Lin, Y.C., Müller, M., and Binder, K. (2004) *J. Chem. Phys.*, **121**, 3816.

126 Müller, M., MacDowell, L.G., Virnau, P., and Binder, K. (2002) *J. Chem. Phys.*, **117**, 5480.

127 Allen, M.P. and Tildesley, D.J. (1987) *Computer Simulation of Liquids*, Clarendon Press, Oxford.

128 Beeman, D. (1976) *J. Comput. Phys.*, **20**, 130.

129 Noakes, J.L. (1998) *J. Aust. Math. Soc. A*, **64**, 37.

130 Ewald, P. (1921) *Ann. Phys.*, **369**, 253.

131 Darden, T.A., York, D.M., and Pedersen, L.G. (1993) *J. Chem. Phys.*, **98**, 8345.

132 Hockney, R. and Eastwood, J. (1981) *Computer Simulation using Particles*, McGraw-Hill, New York.

133 Constanciel, R. and Contreras, R. (1984) *Theor. Chim. Acta*, **65**, 1.

134 Car, R. and Parrinello, M. (1985) *Phys. Rev. Lett.*, **55**, 2471.

135 Evans, D.J. and Morriss, G.P. (1984) *Phys. Rev. A*, **30**, 1528.

136 Ladd, A.J.C. (1984) *Mol. Phys.*, **53**, 459.

137 Murat, M. and Grest, G.S. (1989) *Phys. Rev. Lett.*, **63**, 1074.

138 Evans, D.J. and Morriss, G.P. (1990) *Statistical Mechanics of Nonequilibrium Liquids*, Academic Press, London.

139 Grest, G.S. (1997) *Curr. Opin. Colloid Interface Sci.*, **2**, 271.

140 Doyle, P.S., Shafeh, E.S.G., and Gast, A.P. (1997) *Phys. Rev. Lett.*, **78**, 1182; Doyle, P.S., Shafeh, E.S.G., and Gast, A.P. (1998) *Macromolecules*, **31**, 5474.

141 Grest, G.S. (1999) *Advances in Polymer Science*, vol. **138** (ed. S. Granick), Springer, Berlin, p. 149.

142 Kreer, T., Müser, M.H., Binder, K., and Klein, J. (2001) *Langmuir*, **17**, 7804.

143 Irfachsyad, D., Tildesley, D., and Malfreyt, P. (2002) *Phys. Chem. Chem. Phys.*, **4**, 3008.

144 Kreer, T. and Müser, M.H. (2003) *Wear*, **254**, 827.

145 Kreer, T., Binder, K., and Müser, M.H. (2003) *Langmuir*, **19**, 7551.

146 Cifre, J.G.H., Hess, S., and Kröger, M. (2004) *Macromol. Theory Simul.*, **13**, 748.

147 Goujon, F., Malfreyt, P., and Tildesley, D.J. (2004) *Phys. Chem. Chem. Phys.*, **5**, 457; Goujon, F., Malfreyt, P., and Tildesley, D.J. (2005) *Mol. Phys.*, **103**, 2675; Goujon, F., Malfreyt, P., and Tildesley, D.J. (2008) *J. Chem. Phys.*, **129**, 034902.

148 Daivis, P.J. and Todd, B.D. (2006) *J. Chem. Phys.*, **124**, 194103.

149 Pastorino, C., Binder, K., Kreer, T., and Müller, M. (2006) *J. Chem. Phys.*, **124**, 064902.

150 Pastorino, C., Kreer, T., Müller, M., and Binder, K. (2007) *Phys. Rev. E*, **76**, 026706.

151 Dimitrov, D.I., Milchev, A., and Binder, K. (2007) *J. Chem. Phys.*, **127**, 084905.

152 Todd, B.D. and Daivis, P.J. (2007) *Mol. Simul.*, **33**, 189.

153 Hoogerbrugge, P.J. and Koelman, J.M.V.A. (1992) *Europhys. Lett.*, **19**, 155.

154 Koelman, J.M.V.A. and Hoogerbrugge, P.J. (1993) *Europhys. Lett.*, **21**, 369.

155 Espanol, P. (1995) *Phys. Rev. E*, **52**, 1734.

156 Espanol, P. and Warren, P. (1995) *Europhys. Lett.*, **30**, 191.

157 Schlijper, A.G., Hoogerbrugge, P.J., and Manke, C.W. (1995) *J. Rheol.*, **39**, 567.

158 Kong, Y., Manke, C.M., Madden, W.G., and Schlijper, A.G. (1997) *Baltzer. Tribol. Lett.*, **3**, 133.

159 Bonet Avalos, J. and Mackie, M. (1997) *Europhys. Lett.*, **40**, 141.

160 Espanol, P. (1994) *Europhys. Lett.*, **40**, 631.

161 Novik, K.E. and Coveney, P.V. (1997) *Int. J. Mod. Phys. C*, **8**, 909.

162 Boek, E.S., Coveney, P.V., Lekkerkerker, H.N.W., and van der Schoot, P. (1997) *Phys. Rev. E*, **55**, 3124.

163 Ripoll, M., Espanol, P., and Ernst, M.H. (1999) *Int. J. Mod. Phys. C*, **9**, 1329.

164 Jury, S.I., Bladon, P., Krishna, S., and Cates, M.E. (1999) *Phys. Rev. E*, **59**, R2535.

165 Lowe, C.P. (1999) *Europhys. Lett.*, **47**, 145.

166 Dzwinel, W. and Yuen, D. (2000) *Int. J. Mod. Phys. C*, **11**, 1.

167 Spenley, N.A. (2000) *Europhys. Lett.*, **49**, 534.

168 Besold, G., Vattulainen, I., Karttunen, M., and Polson, J. (2000) *Phys. Rev. E*, **62**, R7611.

169 Shardlow, T. (2003) *SIAM J. Sci. Comput.*, **24**, 1267.

170 Soddemann, T., Dünweg, B., and Kremer, K. (2003) *Phys. Rev. E*, **68**, 046702.

171 Symeonidis, V. and Karniadakis, G.E. (2006) *J. Comput. Phys.*, **218**, 82.

172 Noguchi, H., Kikuchi, N., and Gompper, G. (2007) *Europhys. Lett.*, **78**, 10005.

173 Malevanets, A. and Yeomans, J.M. (2000) *Europhys. Lett.*, **52**, 231.

174 Malevanets, A. and Kapral, R. (2000) *J. Chem. Phys.*, **112**, 7260.

175 Ihle, T. and Kroll, D.M. (2001) *Phys. Rev. E*, **63**, 020201; Ihle, T. and Kroll, D.M. (2003) *Phys. Rev. E*, **67**, 066705.

176 Ripoll, M., Mussawisade, K., Winkler, R.G., and Gompper, G. (2004) *Europhys. Lett.*, **68**, 106.

177 Mussawisade, K., Ripoll, M., Winkler, R.G., and Gompper, G. (2005) *J. Chem. Phys.*, **123**, 144905.

178 Padding, J.T., Wysocki, A., Löwen, H., and Louis, A.A. (2005) *J. Phys.: Condens. Matter*, **17**, S3393.

179 Lee, S.H. and Kapral, R. (2006) *J. Chem. Phys.*, **124**, 214901.

180 Ripoll, M., Winkler, R.G., and Gompper, G. (2006) *Phys. Rev. Lett.*, **96**, 188302; Ripoll, M., Winkler, R.G., and Gompper, G. (2007) *Eur. Phys. J., E*, **23**, 349.

181 Watari, N., Makino, M., Kikuchi, N., Larson, R.G., and Doi, M. (2007) *J. Chem. Phys.*, **126**, 094902.

182 Ladd, A.J.C. (1994) *J. Fluid Mech.*, **271**, 285; Ladd, A.J.C. (1994) *J. Fluid Mech.*, **271**, 311.

183 Ahlrichs, P. and Dünweg, B. (1989) *Int. J. Mod. Phys. C*, **9**, 1429; Ahlrichs, P. and Dünweg, B. (1999) *J. Chem. Phys.*, **111**, 8225.

184 Succi, S. (2001) *The Lattice Boltzmann Equation for Fluid Dynamics and Beyond*, Oxford University Press, New York.

185 Chatterji, A. and Horbach, J. (2005) *J. Chem. Phys.*, **122**, 184903.

186 Dünweg, B. (1993) *J. Chem. Phys.*, **99**, 6977.

187 Junghans, C., Praprotnik, M., and Kremer, K. (2008) *Soft Matter*, **4**, 156.

188 Monaghan, J.J. (1992) *Annu. Rev. Astron. Astrophys.*, **30**, 543.

189 Zimm, B.H. (1956) *J. Chem. Phys.*, **24**, 269.

190 189. Spirin, L., Galuschko, A., Kreer, T., and Binder, K., and Baschnagel, J.,in preparation.

191 Usta, O.B., Butler, J.E., and Ladd, A.J.C. (2007) *Phys. Rev. Lett.*, **98**, 090831.

192 Theodorou, D.N. and Suter, U.W. (1985) *Macromolecules*, **18**, 1467.

193 Moe, N.E. and Ediger, M.D. (1996) *Polymer*, **37**, 1787.

194 Harmandaris, V.A., Mavrantzas, V.G., and Theodorou, D.N. (1998) *Macromolecules*, **31**, 7934.

195 Yao, S. (2000) *Nihon Reoroji Gakk.*, **28**, 159.

196 Fukui, K., Sumpter, B.G., Barnes, M.D., and Noid, D.W. (2000) *Macromolecules*, **33**, 5982.

197 Bicerano, J. (2002) *Prediction of Polymer Properties*, 3rd edn, Marcel Dekker, New York.

198 Soldera, A. and Metatla, N. (2006) *Phys. Rev. E*, **74**, 061803.

199 Clancy, T.C., Jang, J.H., Dhinojwala, A., and Mattice, W.L. (2001) *J. Phys. Chem. B*, **105**, 1493.

200 Smith, G.D., Borodin, O., and Paul, W. (2002) *J. Chem. Phys.*, **117**, 10350.

201 Makrodimitri, Z.A., Raptis, V.E., and Economou, I.G. (2006) *J. Phys. Chem. B*, **110**, 16047.

202 Sun, H. (1995) *Macromolecules*, **8**, 701–712.

203 Heinz, H., Koerner, H., Anderson, K.L., Vaia, R.A., and Farmer, B.L. (2005) *Chem. Mater.*, **17**, 5658.

204 Billeter, M., Guntert, P., Luginbuhl, P., and Wuthrich, K. (1996) *Cell*, **85**, 1057.

205 Clancy, T.C. and Mattice, W.L. (1999) *Comp. Theor. Polym. Sci.*, **9**, 261.

206 Elcock, A.H., Sept, D., and McCammon, J.A. (2001) *J. Phys. Chem. B*, **105**, 1504.

207 Harmandaris, V.A., Angelopoulou, D., Mavrantzas, V.G., and Theodorou, D.N. (2002) *J. Chem. Phys.*, **116**, 7656.

208 Jo, W.H. and Yang, J.S. (2002) *Adv. Polym. Sci.*, **156**, 1.

209 Gestoso, P. and Brisson, J. (2003) *Polymer*, **44**, 2321.

210 Gestoso, P. and Brisson, J. (2003) *Polymer*, **44**, 7765.

211 Faller, R. (2004) *Macromolecules*, **37**, 1095.

212 Wagner, K.G., Maus, M., Kornherr, A., and Zifferer, G. (2005) *Chem. Phys. Lett.*, **406**, 90.

213 Ganazzoli, F. and Raffaini, G. (2005) *Phys. Chem. Chem. Phys.*, **7**, 3651.

214 Genix, A.C., Arbe, A., Alvarez, F., Colmenero, J., Willner, L., and Richter, D. (2005) *Phys. Rev. E*, **72**, 031808.

215 Capaldi, F., Rutledge, G.C., and Boyce, M.C. (2005) *Macromolecules*, **38**, 6700.

216 Makrodimitri, Z.A., Dohrn, R., and Economou, I.G. (2007) *Macromolecules*, **40**, 1720.

217 Abou-Rachid, H., Lussier, L.S., Ringuette, S., Lafleur-Lambert, X., Jaidann, M., and Brisson, J. (2008) *Propell. Explos. Pyrotech.*, **33**, 301.

218 Jaidann, M., Abou-Rachid, H., Lafleur-Lambert, X., Lussier, L.S., Gagnon, N., and Brisson, J. (2008) *Polym. Eng. Sci.*, **48**, 1141.

219 Heinz, H. and Suter, U.W. (2004) *J. Phys. Chem. B*, **108**, 18341.

220 Heinz, H. (2007) *Mol. Simul.*, **33**, 747.

221 Binder, K., Baschnagel, J., and Paul, W. (2003) *Progr. Polym. Sci.*, **28**, 115.

222 Heinz, H., Vaia, R.A., and Farmer, B. (2006) *J. Chem. Phys.*, **124**, 224713.

223 Müller-Plathe, F. (2002) *ChemPhysChem*, **3**, 754.

224 Faller, R. (2004) *Polymer*, **45**, 3869.

225 Sun, Q. and Faller, R. (2006) *J. Chem. Theor. Comput.*, **2**, 607.

226 Fermeglia, M. and Pricl, S. (2007) *Prog. Org. Coat.*, **58**, 187.

227 Cosoli, P., Scocchi, G., Pricl, S., and Fermeglia, M. (2008) *Microporous Mesoporous Mater.*, **107**, 169.

228 Herrebout, W.A., van der Veken, B.J., Wang, A., and Durig, J.R. (1995) *Phys. Chem.*, **99**, 578.

229 Prathab, B. and Aminabhavi, T.M. (2007) *J. Polym. Sci B: Polym. Phys.*, **45**, 1260.

230 Beier, C. and Steinhoff, H.J. (2006) *Biophys. J.*, **91**, 2647.